Universität zu Köln
Institute for Theoretical Physics

Rydberg physics of ytterbium atoms

Jonas Cieslik

A thesis submitted for partial fulfillment of the requirements for the Master of Science

5.6.2023

Thesis Advisor: Prof. Dr. David Gross

Second Examiner: Prof. Dr. Sebastian Hofferberth

Contents

Chapter 1

Overview

In this thesis we will look at an empirical description of complicated spectra of divalent atoms such as strontium, ytterbium, erbium or dysprosium. Specifically, we will look at the so-called "Multichannel Quantum Defect Theory" and use it to calculate Rydberg series of divalent atoms.

These series contain Rydberg states, which are states with high principal quantum number [1]. Atoms in these states are relevant to many areas of physics research because they exhibit many unique properties, due to their exaggerated features compared to conventional atoms. They are often combined with laser cooling and trapping techniques to form the field of "cold Rydberg atoms", which has applications in quantum optics and quantum information [2].

An interesting property of Rydberg atoms is the Rydberg blockade, a mechanism that inhibits the excitation of more than one Rydberg atom within a certain radius by shifting the Rydberg state of the other atom out of resonance [3]. Such an interaction between Rydberg atoms can be used to mediate an interaction between photons. After a photon creates a Rydberg excitation -within the blockade radius - other atoms cannot be excited, which changes certain absorption dynamics. This is used, for example, in quantum computing, where an excitation scheme with a Rydberg blockade is utilized

to implement multi-qubit gates for qubits encoded in the levels of an atom [4]. This makes Rydberg atoms an interesting platform for neutral atom quantum computing.

In recent years, many of these cold Rydberg experiments have started to cool divalent Rydberg atoms, as opposed to the simpler alkali atoms [5]. This is because divalent atoms have weak intercombination transitions from singlet to triplet with very narrow linewidths, allowing them to be cooled to lower Doppler temperatures in a magneto-optical trap. However, these atoms posses complicated atomic spectra compared to alkali metals and they cannot be solved ab initio.

We therefore consider "Multichannel Quantum Defect Theory", which is an empirical approach based on spectroscopic data, which allows us to understand the complicated spectra of divalent atoms and to approximate the wave function of Rydberg states.

In the next chapter we start by looking at a simpler case of multichannel quantum defect theory, simply called "Quantum Defect Theory" (QDT). It describes atoms with one valence electron, as opposed to two, and has long been used to describe the alkalis. It also provides the conceptual foundation for multichannel quantum defect theory.

In the third chapter we then introduce multichannel quantum defect theory and give the necessary theoretical background for empirically calculating the energy states of divalent atoms such as ytterbium and strontium.

Then, in the following chapter, we will look at a recent study of MQDT conducted on strontium and try to replicate its results. We find significant discrepancies, which lead us to calculate three of these series ourselves. This is done in chapter five, where we calculate the energy levels in strontium ourselves. We present our fitting procedure used to fit three different Rydberg series.

In the final chapter we will look at MQDT analysis of ytterbium, which is the relevant atom for the laboratory in which this thesis was written.

Lastly, the appendix of this thesis contains a description of an absorption imaging setup for the laboratory's ytterbium experiment, which was built as part of this thesis.

Chapter 2

Quantum Defect Theory

In this chapter we will look at quantum defect theory, which allows the spectra of alkali metals to be described in terms of quantum defects δ_l. These defects lead to a deviation from the well-known hydrogen spectrum, depending on the angular quantum number l of the valence electron. Quantum defect theory also serves as the basis for the multichannel quantum defect theory of more complex divalent atoms, which we will look at in the next chapter.

2.1 The Hydrogen Atom

In quantum mechanics the hydrogen atom is modelled by an electron orbiting a proton core in a Coulomb potential $V_{\text{Coulomb}}(r) = -\frac{e^2}{4\pi\epsilon_0}\frac{1}{r}$. This system can be solved analytically. It gives the stationary wave function $\Psi_{nlm}(r,\theta,\phi)$ of the electron, with eigenenergies E_n:

$$H\Psi_{nlm} = E_n\Psi_{nlm}, \text{ with:} \tag{2.1}$$

$$\Psi_{nlm}(r,\theta,\phi) = R_{nl}(r)\cdot Y_{lm}(\theta,\phi) \text{ and} \tag{2.2}$$

$$E_n = -\frac{\alpha^2 m_e c^2}{2}\frac{hc}{n^2} = -R\frac{hc}{n^2} = -13.6\,\text{eV}\frac{1}{n^2}\,. \tag{2.3}$$

n is called the principal quantum number and takes only positive integer values, giving the energies of the bound states of the electron. $Y_{lm}(\theta, \phi)$ is a spherical harmonic function and the quantum numbers $l = 0, 1, 2, ..., n-1$ and $m = -l, ..., l$ give the orbital angular momentum and its projection on the z-axis [6].

2.2 Alkalis

However, atoms more complex than hydrogen exhibit many-particle interactions, and it is no longer possible to solve the full Schrödinger equation analytically. To describe the spectra of alkali metals (listed in Table 2.1), the Swedish physicist Johannes Rydberg realised that Equation 2.3 could be corrected by so-called quantum defects δ_l, such that the electron energies $E_{n,l}$ become dependent on the angular momentum l of the valence electron of the alkali atom.

Lithium	$1s^2\ 2s^2$
Sodium	$1s^2\ 2s^2\ 2p^6\ 3s$
Potassium	$1s^2\ 2s^2\ 2p^6\ 3s^2\ 3p^6\ 4s$
Rubidium	$1s^2\ 2s^2\ 2p^6\ 3s^2\ 3p^6\ 3d^{10}\ 4s^2\ 4p^6\ 5s$
Caesium	$1s^2\ 2s^2\ 2p^6\ 3s^2\ 3p^6\ 3d^{10}\ 4s^2\ 4p^6\ 4d^{10}\ 5s^2\ 5p^6\ 6s$
Francium	[Rn] $7s^1$

Table 2.1: Alkali atoms and their electron configuration.

As we will show, the spectrum for alkalis can be written:

$$E_{nl} = -\frac{Rhc}{(n-\delta_l)^2}\,, \tag{2.4}$$

where we made the substitution $n \to n - \delta_l$ from Equation 2.3.
We will now look at the alkali atoms more qualitatively and ultimately derive the formula of Equation 2.4:

2.3 Radial Schrödinger equation

By the usual prescription of quantum mechanics, the wave function $\Psi_{nlm}(\vec{r})$ of the valence electron is an eigenfunction of the time-independent Schrödinger equation. In a spherically symmetric potential, the wave function can be separated into a radial and an angular part:

$$\Psi(r,\theta,\phi) = \frac{u(r)}{r} Y_l^m(\theta,\phi) \tag{2.5}$$

and the radial part obeys the radial Schrödinger equation:

$$\left[-\frac{\hbar}{2m}\frac{d^2}{dr^2} + \frac{\hbar^2 l(l+1)}{2mr^2} + V(r) \right] u(r) = E u(r)\,. \tag{2.6}$$

One strategy for calculating the energy spectrum for alkalis is to model the potential acting on the valence electron, by a purely radial potential $V_l(r)$, which depends only on the distance of the electron from the core and its angular momentum l. Many parametrisations of this model potential have been investigated, for example in [7], [8]:

$$V_l(r) = -2\frac{Z_l(r)}{r} - \frac{\alpha_c}{r^4}\left[1 - e^{-(r/r_c)^6}\right]\,, \tag{2.7}$$

$$Z_l(r) = 1 + (Z-1)e^{-a_1 r} - r(a_3 + a_4 r)e^{-a_2 r}\,, \tag{2.8}$$

where α_c is the static dipole polarizability, Z the nuclear charge and r_c a cut off radius. This can be solved numerically and the parameters a_1, a_2, a_3 and a_4 may be determined by fitting calculated spectra to those obtained experimentally.

2.4 Quantum Defect Theory

Another approach to finding the energy levels for non-hydrogenic potentials is called quantum defect theory. It makes use of the fact that more highly excited electrons traverse a large domain of space for which their distance to the core is larger than some value r_c, $r \geq r_c$, Fig. 2.1. In this region, $V_l(r)$

would be equivalent to a pure Coulomb potential, as the charges of the singly positively charged core are screened to form an effective Coulomb potential acting at these larger distances:

$$V_{\text{core}}(r) \xrightarrow{r \geq r_c} V_{\text{Coulomb}}(r) = -\frac{Z}{r}\,, \tag{2.9}$$

where we have used atomic units: $m_e = e = \hbar = \frac{1}{4\pi\epsilon_0} = 1$.

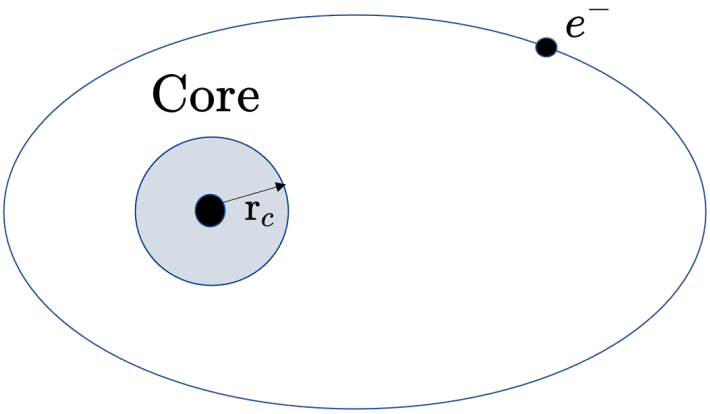

Figure 2.1: Simplified sketch of a valence electron orbiting an atom core. Outside of the grey core region, the potential is screened to form a Coulomb potential, acting on the valence electron.

This is depicted in Fig. 2.2. At distances below r_c the potential may be deeper than the pure Coulomb potential, but at large distances this becomes negligible and we can ignore the effects of the interactions with all of the other electrons in the core.

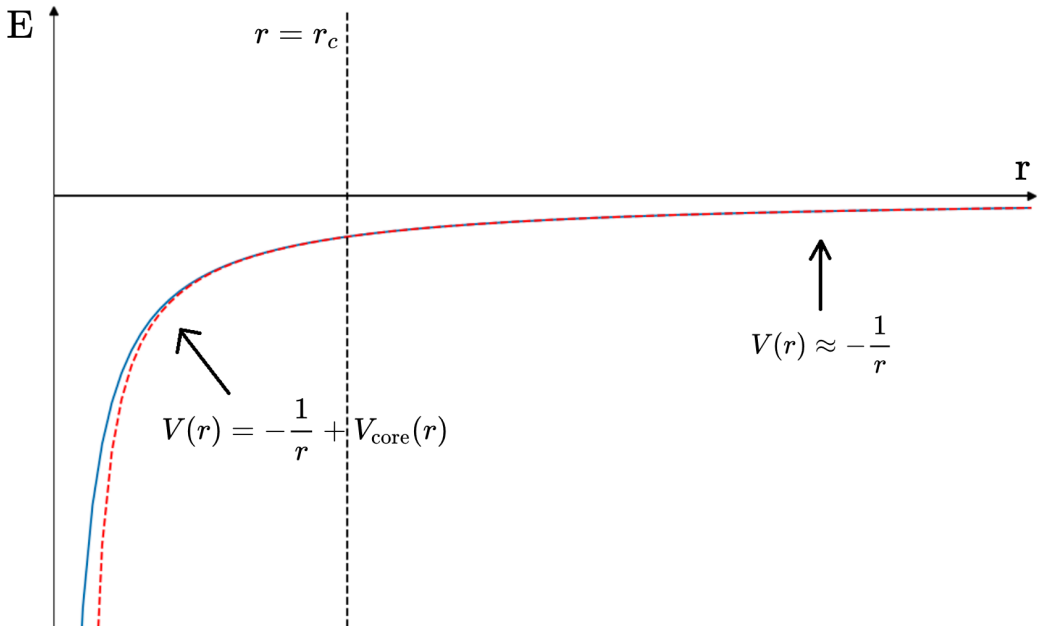

Figure 2.2: Approximation of the potential by a Coulomb potential.

Solutions

It has been shown that this Coulomb potential is generally solved by two linearly independent functions, called confluent hypergeometric functions [9]. Most importantly, these functions f and g have the following behaviour for $E = \frac{1}{2}k^2 > 0$ (atomic units):

$$f(l, E, r) \to 0 \text{ as } r \to 0\,, \tag{2.10}$$

$$g(l, E, r) \to \infty \text{ as } r \to 0 \tag{2.11}$$

and

$$f \to (2/\pi k)^{1/2} \sin\left(kr + \frac{1}{k}\ln r + \alpha_l\right) \text{ as } r \to \infty\,, \tag{2.12}$$

$$g \to (2/\pi k)^{1/2} \cos\left(kr + \frac{1}{k}\ln r + \alpha_l\right) \text{ as } r \to \infty\,, \tag{2.13}$$

with so called Coulomb phase α_l. f is called regular Coulomb function and g is called irregular Coulomb function.

Since they are linearly independent, any valid wave function for $r \geq r_c$ must be a linear combination of these two functions. This superposition is written as

$$u_{nl}(r) = \left[\cos\left(\pi\delta_l\right) f(r) + \sin\left(\pi\delta_l\right) g(r)\right] . \tag{2.14}$$

A system with a pure Coulomb potential over the whole range and without core effects, such as hydrogen, would simply be solved by $f(r)$. This is because $f(r)$ obeys the boundary condition, going to zero as $r \to 0$, which $g(r)$ does not.

However, in the case of the alkalis, we only speak of a Coulomb potential for $r \geq r_c$, and this leads to the solution in form of Equation 2.14. Without knowledge of the precise core physics, $u_{nl}(r)$ still has to be continuously matched to the core wave function at $r = r_c$. This mixes some of the $g(r)$ function into the radial wave function $u_{nl}(r)$ and gives rise to the quantum defect δ_l.

Normalisability Condition

We will determine the quantized eigenspectrum of Equation 2.4, by imposing the condition that the wave function must be normalisable.

To utilize this normalisability condition, we consider the regular and irregular Coulomb functions asymptotically and for negative energies $E = -\frac{k^2}{2} = \frac{(i\kappa)^2}{2}$, since these energies give the bound states of the atom. For negative energies, we get by analytic continuation $k \to i\kappa$ [9]:

$$f_{E,l}(r) \to (\pi\kappa)^{-1/2} \left(\sin(\beta) D^{-1} r^{-\nu} e^{\kappa r} - \cos(\beta) D r^{\nu} e^{-\kappa r}\right) , \tag{2.15}$$

$$g_{E,l}(r) \to (\pi\kappa)^{-1/2} \left(\cos(\beta) D^{-1} r^{-\nu} e^{\kappa r} + \sin(\beta) D r^{\nu} e^{-\kappa r}\right) , \tag{2.16}$$

$\nu = \kappa^{-1}$, $\beta = \pi(\nu - l)$ and D is a parameter depending on E and l.

We introduced the abbreviations $a = (\pi\kappa)^{-1/2} D^{-1} r^{-\nu} e^{\kappa r}$ and

$b = (\pi\kappa)^{-1/2} D r^{\nu} e^{-\kappa r}$:

$$f_{E,l}(r) \to \sin(\beta)a - \cos(\beta)b\,, \tag{2.17}$$

$$g_{E,l}(r) \to \cos(\beta)a + \sin(\beta)b\,. \tag{2.18}$$

These asymptotes can be plugged into Equation 2.14:

$$u_{nl}(r) = \left[\cos(\pi\delta_l)f(r) + \sin(\pi\delta_l)g(r)\right]\,, \tag{2.19}$$

$$\to \left[\cos(\pi\delta_l)\left(\sin(\beta)a - \cos(\beta)b\right) + \sin(\pi\delta_l)\left(\cos(\beta)a + \sin(\beta)b\right)\right] \tag{2.20}$$

$$= a\left(\cos(\pi\delta_l)\sin(\beta) + \sin(\pi\delta_l)\cos(\beta)\right)$$

$$- b\left(\cos(\pi\delta_l)\cos(\beta) + \sin(\pi\delta_l)\sin(\beta)\right) \tag{2.21}$$

$$= a\sin(\pi\delta_l + \beta) - b\cos(\pi\delta_l + \beta)\,. \tag{2.22}$$

Finally, to ensure normalisability of $u_{nl}(r)$, the diverging term $e^{\kappa r}$ contained in a must be made to vanish. This is accomplished by making $\sin(\beta + \pi\delta_l)$ vanish. Thus:

$$\pi(\nu - l + \delta_l) = N\pi\,, N \in \mathbb{Z}\,, n = N + l \tag{2.23}$$

and it follows that:

$$\boxed{E_{nl} = -\frac{\kappa^2}{2} = -\frac{1}{2\nu^2} = -\frac{1}{2(n-\delta_l)^2}}\,, \tag{2.24}$$

giving the famous Rydberg formula in atomic units, with the angular momentum dependent quantum defect δ_l.

This is obviously only approximate, since we have not considered things such as core polarization, or relativistic effects. The full wave function is given by Equation 2.5:

$$\Psi_{nlm}(\theta,\phi,r) = \frac{Y_{lm}(\theta,\phi,r)\left[f_{E,l}(r)\cos(\pi\delta_l) + g_{E,l}(r)\sin(\pi\delta_l)\right]}{r}\,. \tag{2.25}$$

One method of calculating δ_l is to numerically solve the model potential

Hamiltonian, given by Equation 2.6 for the small core region $r \leq r_c$ and match it to $u_{nl}(r)$ of Equation 2.14 at $r = r_c$, requiring continuity.

2.5 Rydberg series

Equation 2.24 leads to various Rydberg states with common quantum number l forming a "Rydberg series" with a deviation δ_l from the quantum number n of hydrogen. The Rydberg series for $l = s, p, d, f, g$ of sodium are depicted in Fig. 2.3 and listed in Table 2.2. One can see that the defect is strongest for smaller angular momenta since for those values the electron is most likely to be in the core region and therefore interact with the unscreened part of the potential.

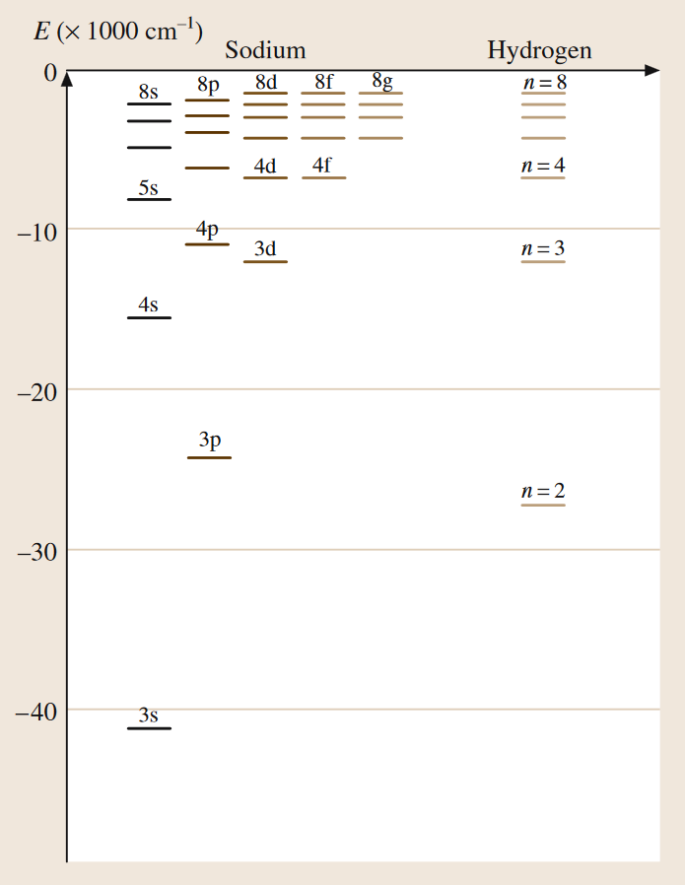

Figure 2.3: Rydberg series in sodium compared to hydrogen, taken from [10].

	n=3	4	5	6	7	8
l=s	1.373	1.357	1.352	1.349	1.348	1.351
p	0.883	0.867	0.862	0.859	0.858	0.857
d	0.010	0.011	0.013	0.011	0.009	0.013
f	-	0.000	-0.001	-0.008	-0.012	-0.015

Table 2.2: Quantum defects δ_l for sodium [11]. They show a strong l dependence and a weak n dependence.

In the next chapter we turn our attention to multichannel quantum defect theory to describe divalent atoms. It relies on the same Coulomb approximation, but the additional core electron must be taken into account and can lead to perturbations of a Rydberg series.

Chapter 3

Multichannel Quantum Defect Theory

Overview

In the introduction of this thesis, we have shown that atoms with two valence electrons are used in a wide range of cold atom experiments. This makes it desirable for many physicists to understand the atomic spectra of these atoms and how they are formed. It turns out, however, that a theoretical description is much more complex, than for the alkalis in the previous chapter. This is due to the fact that divalent Rydberg atoms have doubly excited states (e.g. 5sns $\rightarrow$ 4dnd) which cause a departure from the simpler one-electron physics. If these doubly excited states (perturbers) coincide in energy, parity and total angular momentum, with a state of a Rydberg series, they can cause perturbations that are not present in the single-valence case where there are no doubly excited states. We will se that perturbers can mix into wave function of the bound states of a series, leading to the presence of transitions which would normally be dipole forbidden.

These perturbations lead to a quantum defect which varies for each state m of a given Rydberg series. As we will see, the energy spectrum can then be described by the non-integer quantum numbers $\nu_i^{(m)}$, which are given

relative to an ionisation limit labelled by i. We will see that a state m has the energy:

$$E^{(m)} = I_i - \frac{\hat{R}}{\left(\nu_i^{(m)}\right)^2}, \tag{3.1}$$

with Rydberg constant $\hat{R} = \frac{\alpha^2 c M m_e}{2h(m_e+M)}$ and ionisation limit I_i (We have multiple energy levels, labelled by m, which can be expressed relative to different ionisation limits, labelled by i).

This is in contrast to the last chapter, where the energies of atoms with one valence electron were given by a constant quantum defect δ_l and an integer quantum number n: $E_{n,l} = I_i - \frac{\hat{R}}{(n-\delta_l)^2}$, which in the divalent case is modified to the more general $\nu_i^{(m)}$ in the denominator.

Lu-Fano plot and Perturbations

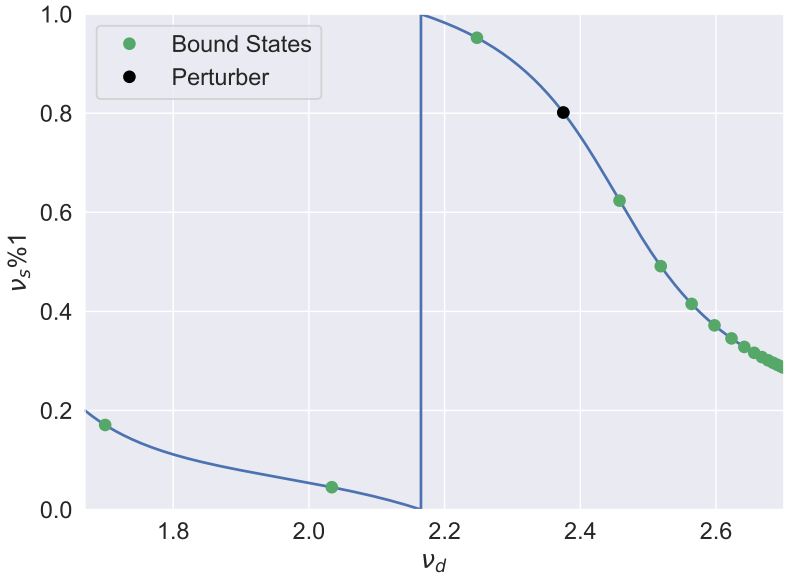

Figure 3.1: Lu-Fano plot of Sr $^1P_1$, quantum defects relative to $4d$ and $5s$ ionisation limits in strontium [12].

In the plot above, Fig. 3.1 we see a so-called Lu-Fano plot of the $^1P_1$ series of strontium. The principal quantum numbers $\nu_i^{(m)}$ are written with respect to two different ionisation limits: On the x-axis ν_d with respect to the $4d = 60\,628.26\,\mathrm{cm}^{-1}$ limit and on the y-axis ν_s modulo one with respect to the $5s = 45\,932.1982\,\mathrm{cm}^{-1}$ limit. In addition, the values on the y-axis are plotted modulo one, which visualises the resonance features due to perturbers:

For the unperturbed alkalis of the previous chapter, which have Rydberg series with $\nu = n - \delta_l$ (see Equation 2.24), such a plot would have the constant values $\nu_i \% 1 = (n - \delta_l) \% 1 = \text{const.}$ on the y- axis. This would lead to the bound states forming a straight, horizontal line in the Lu-Fano plot. However, in Fig. 3.1 we see a clear deviation from this straight line, which is caused by the doubly excited perturbation shown in black.

In order to explain this behaviour more quantitatively, and to eventually calculate bound states of a series, given by $\nu_i^{(m)}$, we will use of multichannel quantum defect theory (MQDT). This will enable us to derive two mathematical constraints on $\nu_i^{(m)}$, given by Equation 3.19 and the Equation 3.18, which can be used to calculate bound states of a Rydberg series.

3.1 Multichannel Quantum Defect Theory

MQDT was first studied in 1955 [13] and many approaches have been used since then. For the purpose of this thesis, we have looked at more recent work [12], some of whose results we will try to reproduce in the next chapter.

3.1.1 Schrödinger equation

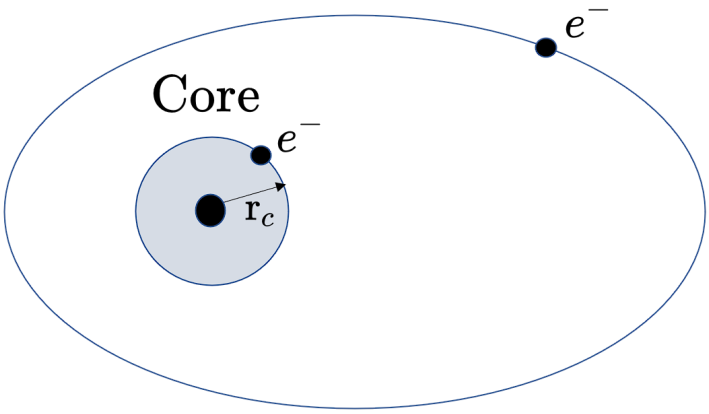

Figure 3.2: Simplified sketch of a valence electron orbiting an atom core with a second valence electron. Outside of the grey core region, the potential is screened to form a Coulomb potential, acting on the excited electron.

Similar to the case of quantum defect theory in the previous chapter, we exploit the fact that for large distances, $r \geq r_c$ between the Rydberg electron and the core, the Rydberg electron is dominated by a Coulomb interaction of the form $V(r) = -\frac{1}{r}$. Applying the Schrödinger equation, the radial wave function of the active electron therefore satisfies the Coulomb potential Hamiltonian at distances $r \geq r_c$:

$$\left[-\frac{1}{2\mu}\frac{d^2}{dr^2} + \frac{l_i(l_i+1)}{2\mu r^2} - \frac{1}{r}\right]\phi_i(r) = \epsilon_i\phi_i(r)\ . \tag{3.2}$$

The equation is given in atomic units, $\mu = \frac{M_{core}m_{e^-}}{M_{core}+m_{e^-}}$ is the reduced mass of the system and ϵ_i is the energy of the active electron in the channel, defined relative to the ionisation limit I_i and in units of wavenumber: $\epsilon_i = (E - I_i)hc$.

This approach is equivalent to the single valence electron case of section 2.6, but introduces an additional label i to the eigenfunctions. This label keeps track of the configuration of core and valence electron, such as: $i = 4dnd\,^3D_1$ or $i = 5sns\,^1S_0$. These configurations of core electron and Rydberg

electron are called channels and form the basis of the wave function. It is important to note that MQDT does not give any information about the term symbol of a states and in some cases perturbers and their channels are best described in LS-coupling $^{2S+1}L_J$, while in other cases jj-coupling $(j_1, j_2)_J$ is more appropriate.

Crucially, this Hamiltonian, valid at large distances $r \geq r_0$, does not couple multiple channels i and j with each other, as the full Hamiltonian, valid for all distances, does. This allows us to use a basis consisting of $\phi_i(r)$, as opposed to the much larger $\phi_{ij}(r)$ basis of the interacting case.

Solutions

Now, analogous to the case of a single valence electron, any solution to the Schrödinger equation can be written as a linear superposition of two linearly independent solutions, which we take to be the regular and irregular Coulomb functions $f(l_i, \epsilon_i, r)$ and $g(l_i, \epsilon_i, r)$ respectively. They have the asymtotic properties:

$$f(l_i, \epsilon_i, r) \to 0 \text{ as } r \to 0, \text{ regular Coulomb function}\,,$$
$$g(l_i, \epsilon_i, r) \to \infty \text{ as } r \to 0, \text{ irregular Coulomb function}\,.$$

Note: Since we will use these only up to r_c we need not be concerned with the divergence of g as $r \to \infty$. The solutions of the Schrödinger equation are then:

$$\phi_i(r) = \left[f(l_i, \epsilon_i, r)\cos\theta_i + g(l_i, \epsilon_i, r)\sin\theta_i\right]\,, r \gg r_c\,. \tag{3.3}$$

The variable θ_i determines the weight of the individual regular and irregular Coulomb functions in the superposition and can be written in terms of an effective principal quantum number ν_i, $\theta_i = \pi\nu_i = \pi(n - \delta_i)$.

3.1.2 Wave Function

In general, the full wave function of the atomic Hamiltonian is a linear superposition of the different channel wave functions $\phi_i(r)$, which form a basis. Thus, if Ψ is the eigenfunction of a state of interest, one can write:

$$\Psi = \frac{1}{r}\hat{\mathcal{A}} \sum_i A_i \phi_i \chi_i \,, \tag{3.4}$$

the functions χ_i describe the angular and spin dependence of the active electron as well as the radial, angular and spin dependence of all other non-Rydberg electrons. $\hat{\mathcal{A}}$ is the antisymmetrization operator needed for indistinguishable fermions, and A_i, the channel fractions, determine the admixture of each channel wave function into the full wave function Ψ .

Boundary Condition at $r = r_c$

We still have to impose the boundary condition at $r = r_c$. To do this, we change to a new basis from $\phi_i\chi_i$, by an unitary, orthogonal transformation $U_{i\alpha}$ and write the so-called scattering modes in it:

$$\psi_\alpha = \left(\frac{1}{r}\hat{\mathcal{A}} \sum_i U_{i\alpha} f(l_i, \epsilon_i, r)\chi_i\right) \cos(\pi\mu_\alpha) - \left(\frac{1}{r}\hat{\mathcal{A}} \sum_i U_{i\alpha} g(l_i, \epsilon_i, r)\chi_i\right) \sin(\pi\mu_\alpha) \,. \tag{3.5}$$

These scattering mode functions can be thought of as the normal modes of the scattering problem. A standing wave enters the core region and in a scattering picture gets reflected with only a phase shift [14]. The composition of the linear combination is not altered by scattering from the ionic core and ψ_α form a new basis set.

We can now write the complete atomic wave function in terms of the scat-

tering modes:

$$\Psi = \sum_i A_i \phi_i \chi_i = \sum_\alpha B_\alpha \psi_\alpha \tag{3.6}$$

and insert the equations 3.3 and 3.5, giving the expression:

$$\begin{aligned}&\sum_i A_i \chi_i g(l_i, \epsilon_i, r) \sin(\pi\nu_i) + \sum_i A_i \chi_i f(l_i, \epsilon_i, r) \cos(\pi\nu_i) = \\ &- \sum_\alpha B_\alpha \sum_i U_{i\alpha} \chi_i g(l_i, \epsilon_i, r) \sin(\pi\mu_\alpha) + \sum_\alpha B_\alpha \sum_i U_{i\alpha} \chi_i f(l_i, \epsilon_i, r) \cos(\pi\mu_\alpha)\,.\end{aligned} \tag{3.7}$$

Equating the coefficients of these expressions gives us constrains on some variables:

$$A_i \cos(\pi\nu_i) = \sum_\alpha U_{i\alpha} B_\alpha \cos(\pi\mu_\alpha)\,, \tag{3.8}$$

$$A_i \sin(\pi\nu_i) = -\sum_\alpha U_{i\alpha} B_\alpha \sin(\pi\mu_\alpha)\,. \tag{3.9}$$

Using unitarity of the Matrix $U_{i\alpha}$, these equations can be written

$$\sum_i U_{i\alpha} A_i \cos(\pi\nu_i) = B_\alpha \cos(\pi\mu_\alpha)\,, \tag{3.10}$$

$$\sum_i U_{i\alpha} A_i \sin(\pi\nu_i) = -B_\alpha \sin(\pi\mu_\alpha)\,. \tag{3.11}$$

Now we multiply the first equation with $\cos(\pi\nu_i)$ and the second with $\sin(\pi\nu_i)$ and add them together. After using $\cos(x)\cos(y) - \sin(x)\sin(y) = \cos(x+y)$ and $\cos(x)^2 + \sin(x)^2 = 1$, we get Equation 3.12.

Next, we multiply Equation 3.10 with $\sin(\pi\nu_i)$ and Equation 3.11 with $\cos(\pi\nu_i)$ and subtract them. Using $\cos(x)\sin(y) + \sin(x)\cos(y) = \sin(x+y)$ gives

Equation 3.13:

$$\sum_i U_{i\alpha} \cos(\pi(\nu_i + \mu_\alpha)) A_i = B_\alpha \,, \tag{3.12}$$

$$\sum_i U_{i\alpha} \sin(\pi(\nu_i + \mu_\alpha)) A_i = 0 \,. \tag{3.13}$$

This resulting system of equations now finally gives us a constraint that will be needed in the calculation of bound states. This is because for a non-trivial solution to exist, one must have a non-vanishing determinant, which gives us the expression:

$$\det(U_{i\alpha} \sin\left(\pi(\nu_i + \mu_\alpha)\right)) = 0 \,. \tag{3.14}$$

This expression constraints ν_i for given $U_{i\alpha}$ and μ_α.

K-Matrix

For further calculations it is advantageous to rewrite Equation 3.13 as

$$\cos(\pi\mu_\alpha) \sum_i [U_{i\alpha} \tan(\pi\nu_i) + \tan(\pi\mu_\alpha) U_{i\alpha}] \cos(\pi\nu_i) A_i = 0 \,, \tag{3.15}$$

which can be brought into the much simpler form of

$$\sum_i [K_{i\alpha} + \delta_{i\alpha} \tan(\pi\nu_i)] a_i = 0 \,, \tag{3.16}$$

$a_i = A_i \cos(\pi\nu_i)$. $K_{i\alpha}$ is known as the K-Matrix or reactance matrix, given by

$$K_{i\alpha} = U^\dagger_{i\alpha} \delta_{\alpha i} \tan(\pi\mu_\alpha) U_{i\alpha} \,. \tag{3.17}$$

This K-Matrix is symmetric since $(ABC)^\dagger = C^\dagger B^\dagger A^\dagger$.

The condition given by Equation 3.14 becomes

$$\boxed{\det\left(K_{i\alpha} + \delta_{i\alpha} \tan(\pi\nu_i)\right) = 0} \,. \tag{3.18}$$

Boundary Condition at $r \to \infty$

So far we have applied boundary conditions close to the atomic core, at $r = r_c$. In addition, we need to impose a second long-range boundary condition, which requires that $\Psi \to 0$ as $r \to \infty$. This leads, analogously to the derivation of equation 2.24, to an additional constraint on the bound state energies:

$$\boxed{E = I_i - \frac{\hat{R}}{\nu_i^2}\,,\; i = 1\,, \ldots\,, N}\,, \tag{3.19}$$

with energies relative to an ionisation limit I_i, given in SI units.

We have now derived two formulas, 3.18 and 3.19, that can be used to calculate the boundstates ν_j. This calculation will be described in the next section.

3.1.3 Finding Bound States via K-Matrix

Assuming that we know the ionisation limits I_i and the coefficients of the $K_{i\alpha}$-matrix, defined by Equation 3.17, we can now use the previously derived formulas to calculate the bound states of a Rydberg series and its quantum numbers ν_j:

$$K_{i\alpha} \to \text{Bound states } \{\nu_i\}\,.$$

This is achieved using the equations 3.18 and 3.19:

$$E = I_i - \frac{\hat{R}}{\nu_i^2},\; i = 1, \ldots, N\,, \tag{3.20}$$

$$\det\left(K_{i\alpha} + \delta_{i\alpha}\tan(\pi\nu_i)\right) = 0\,. \tag{3.21}$$

The principal quantum numbers of a series are mathematically fully determined by the set of $\{\nu_i\}$, which fulfil both equations 3.20 and 3.21, provided we have knowledge of $K_{i\alpha}$. Therefore, finding the solution to both of these equations gives us the bound states $\{\nu_i\}$ of a Rydberg series. Specifically, we

can proceed as follows:

Procedure for calculating bound states

Our series has N relevant channels (one for each perturber that mixes in). For the purpose of calculating the bound state energies, we pick one and label it by j, with the aim of expressing all the other ν_i in terms of it:

$$\nu_i(\nu_j) \text{ for } i \neq j\,. \tag{3.22}$$

This is easily achieved with Equation 3.20, by equating the energies of the j channel with those of the other i channels:

$$I_i - \frac{\hat{R}}{\nu_i^2} = I_j - \frac{\hat{R}}{\nu_j^2}\,, \tag{3.23}$$

which may be rearranged to:

$$\nu_k(\nu_j) = \left[\frac{I_k - I_j}{\hat{R}} + \frac{1}{\nu_j^2}\right]^{-1/2}\,. \tag{3.24}$$

This allows all quantum numbers ν_i to be expressed in terms of the one quantum number ν_j.

Next we substitute each bound state $\nu_i(\nu_j)$, expressed as a function of ν_j, into Equation 3.21 . This results in a function f(ν_j) that depends on only one variable, namely ν_j:

$$f(\nu_j) = \det\left(K_{i\alpha} + \delta_{i\alpha}\tan(\pi\nu_i(\nu_j))\right) = 0, \tag{3.25}$$

where j labels a single channels out of all N channels. Finding the zeros $\{\nu_j\}$ of this function is then equivalent to finding the bound state energies of the series, since both conditions on ν_i, given by equations 3.20 and 3.21 are satisfied.

We therefore have shown how to find the bound state quantum numbers from the zeros $\{\nu_j\}$ of Equation 3.25, assuming knowledge of the $K_{i\alpha}$-matrix.

They are also sufficient to find the so-called channel fractions of the wave function:

3.1.4 Channel Fractions

The so-called normalised channel fractions $\bar{A}_i$ are of great importance. They give the coefficients A_i of the eigenchannel-basis wave function: $\Psi = \frac{1}{r}\hat{\mathcal{A}}\sum_i A_i\phi_i\chi_i$ (Equation 3.4) and provide information about the mixing of individual channels to a given bound state and determine how heavily each channels is weighted.

They can be obtained through the system of equations 3.16:

$$\sum_i [K_{i\alpha} + \delta_{i\alpha}\tan(\pi\nu_i)]a_i = 0\,, \tag{3.26}$$

where $a_i = A_i\cos(\pi\nu_i)$. These equations do not uniquely determine A_i, but it can be shown that each channel i should normalise to ν_i^3 [15]. We therefore define normalised channel fractions $\sum_i \bar{A}_i^2 = 1$ and $\bar{A}_i = \nu_i^{3/2}A_i$, such that A_i can be uniquely determined.

This can be used to calculate a hoist of additional properties such as dipole matrix elements, radiative lifetimes or the Landé g-factors and enables the exploration of properties like Stark maps and general long-range interactions of Rydberg states [12].

3.1.5 Corrections to the K-Matrix

When deriving the K-matrix, we approximated the potential acting on the excited electron as a Coulomb potential. To correct for some of the discrepancies which might arise from such an approximation further parameters μ_i are introduced into the K-matrix. They simply add a term, linear in energy to the diagonal K_{ii} of the K-matrix:

$$K_{ii} + \mu_i \cdot \frac{I_s - E}{I_s}\,, \tag{3.27}$$

where I_s is the first ionisation threshold of the atom.

3.1.6 Two Channel Example

For the sake of clarity, we will give an example of a general two-channel model and show how to calculate the bound state quantum numbers in this case.

An example of a two-channel model is given by the $5snp\,^1P_1$ series of strontium, where the $5snp\,^1P_1$ channel (channel 1) and the $4dnp\,^1P_1$ channel (channel 2) couple due to a perturber labelled by $4d5p\,^1P_1$. Such a series gives us a 2×2 K-matrix with five parameters (assuming energy dependence on the diagonals), namely K_{11}, K_{12}, K_{22}, μ_1 and μ_2:

$$K_{i\alpha} = \begin{array}{c} \\ \text{channel 1} \\ \text{channel 2} \end{array} \begin{array}{c} \begin{array}{cc} \text{channel 1} & \text{channel 2} \end{array} \\ \begin{pmatrix} K_{11} + \mu_1 \frac{I_s - E}{E} & K_{12} \\ K_{12} & K_{22} + \mu_2 \frac{I_s - E}{E} \end{pmatrix} \end{array}$$

Table 3.1: Two channel K-Matrix.

In a two channel series we have two principal quantum numbers ν_1 and ν_2, defined by Equation 3.20, with energies relative to their respective ionisation limits. Now we can proceed as discussed in Section 3.1.3 to calculate these quantum numbers. Applying the procedure introduced in that section, we reduce our system to a single variable, analogous to Equation 3.24:

$$\nu_1(\nu_2) = \left[\frac{I_1 - I_2}{R} + \frac{1}{\nu_2^2} \right]^{-1/2} . \tag{3.28}$$

Next we make Equation 3.21 a function of only ν_2, by plugging in the above

equation 3.28 for ν_1, yielding:

$$\det\left(\begin{bmatrix} K_{11}+\mu_1\frac{I_s-E}{E} & K_{12} \\ K_{12} & K_{22}+\mu_2\frac{I_s-E}{E} \end{bmatrix} + \begin{bmatrix} \tan\left(\pi\left[\frac{I_1-I_2}{R}+\frac{1}{\nu_2^2}\right]^{-1/2}\right) & 0 \\ 0 & \tan(\pi\nu_2) \end{bmatrix}\right)$$
$$:= \det\left(\begin{bmatrix} d_1 & K_{12} \\ K_{12} & d_2 \end{bmatrix}\right) = d_1 d_2 - K_{12}^2 = 0\,. \tag{3.29}$$

Since the whole expression depends only on ν_2, the last expression $d_1 d_2 - K_{12}^2 = 0$ can be solved for the bound state quantum number ν_2. This also allows us to calculate ν_1 by Equation 3.28, which means we have successfully calculated the bound states ν_i.

Visualisation

The process of finding the bound states with the two conditions 3.20 and 3.21 can be visualised by plotting both, Equation 3.28 ("Condition one") and $d_1 d_2 - K_{12}^2 = 0$ ("Condition two"), algebraically rearranged into the form $\nu_1(\nu_2)$. Their intersections satisfy both conditions and give the bound states, as depicted in Fig. 3.3.

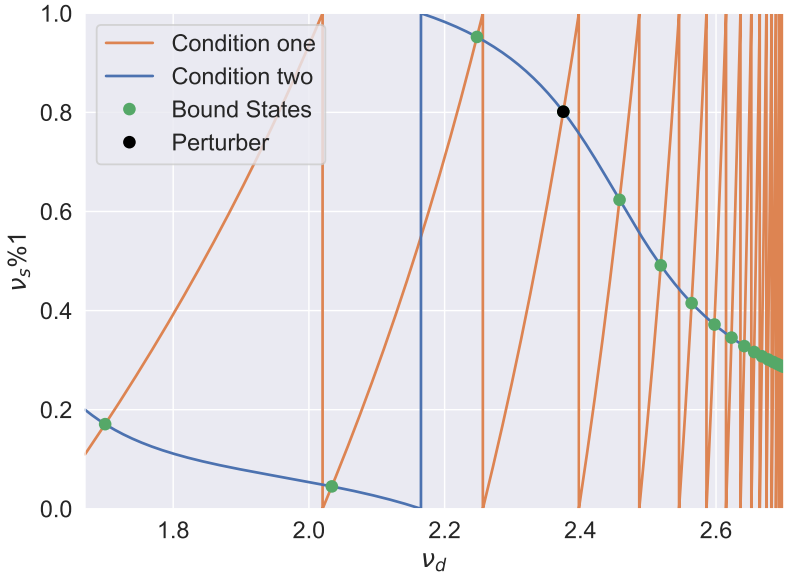

Figure 3.3: Points that full fill both conditions 3.28 and 3.29 are boundstates.

Channel Fractions

For the channel fractions $\bar{A}_i$ of a two-channel series, introduced in section 3.1.4, we can solve Equation 3.26. The channel fractions are given by:

$$\bar{A}_1 = \nu_1^{\frac{3}{2}} \left[\nu_1^3 + \frac{\nu_2^3 (K_{11} + \tan(\pi\nu_1))^2}{K_{12}^2} \left(\frac{\cos(\pi\nu_1)}{\cos(\pi\nu_2)} \right)^2 \right]^{-1/2} , \tag{3.30}$$

$$\bar{A}_2 = -\left(\frac{\nu_2}{\nu_1} \right)^{3/2} \frac{(K_{11} + \tan \pi\nu_1)}{K_{12}} \frac{\cos \pi\nu_1}{\cos \pi\nu_2} \tilde{A}_1 \, . \tag{3.31}$$

In the next section we will return to the general N-channel case and turn our attention towards determining the K-matrix.

3.2 Determining the K-Matrix

We have seen that MQDT allows us to calculate the energy spectrum and the channel fractions of a series of divalent Rydberg atoms. However, we always assumed that we knew the K-matrix parameters and used them in

all these calculations. This is obviously not the case, and although there are attempts to calculate the K-matrix (often called Reactance Matrix) ab initio, these attempts rarely reproduce the series with experimental precision [2]. However, we can use the tools described in this chapter to determine the K-matrix from spectroscopic data:

3.2.1 Fitting the K-Matrix

To obtain the K-matrix we proceed in the opposite way to before, where we used the K-matrix to derive bound states. We take advantage of the fact that we have some knowledge of the bound state energies from spectroscopic measurements and use the bound states to determine the K-matrix empirically:

$$\text{Bound states } \{\nu_i\} \rightarrow K_{i\alpha}$$

The determination of the K-matrix from the bound states is possible by fitting the bound states to the experimental ones and using the K-matrix parameters as fitting parameters:

We use Equation 3.25. As we have shown, this Equation gives a function $f(\nu_j) = \det\left(K_{i\alpha} + \delta_{i\alpha}\tan(\pi\nu_i(\nu_j))\right)$ whose zeros $\{\nu_j\}$ give the bound state energies for some choice of $K_{i\alpha}$. Using the experimentally obtained bound state energies, say $E^{(exp)}$, it is possible to compare these to those obtained by calculation. This comparison is made by a cost function which, for a given $K_{i\alpha}$, compares calculated and measured energies and assigns a cost to them.

This cost can then be minimised numerically, and as the result of a successful minimisation we will get the values of the K-matrix for which the bound states are optimally approximated, and therefore we have determined the K-matrix empirically.

We will proceed to do so in Chapter 5, where we will perform fits for multiple strontium Rydberg series. In that chapter we will also give a more detailed

description of the fitting procedure that was used, and define the cost function that was minimised.

Summary

In this chapter we have discussed the ideas of multichannel quantum defect theory. We introduced the $K_{i\alpha}$-matrix and explained how it can be used to calculate bound states of a divalent Rydberg series, by calculating the zeros of a function, 3.25. We have also introduced the idea of using empirical spectroscopic data, to fit the K-matrix parameters, so that they do not have to be calculated ab initio. In the next chapter we will look at a MQDT study carried out for strontium.

Chapter 4

Strontium MQDT

4.1 Recent MQDT Analysis

For the purpose of this thesis we will now consider a MQDT analysis of strontium. Strontium is an alkaline earth metal with atomic number 38 and two valence electrons. It is used in many cold atom experiments and is a good candidate for an MQDT analysis because the experimental data is known to good precision. It has recently been analysed in [12]. This 2014 paper uses the most recent spectroscopic data of strontium to fit the K-matrix coefficients for different Rydberg series, namely ${}^1S_0, {}^3S_1, {}^1P_1, {}^3P_{0,1,2}, {}^{1,3}D_2, {}^3D_{1,3}$ and ${}^1F_3$.

To gain an understanding of MQDT, we attempted to recreate the spectra of the series in the paper. We proceeded as explained in section 3.1.3, using the the K-matrix calculated in [12] to calculate bound states.

However, when we did this, we found that for some of the series, the fit in the paper was rather imprecise and it did not reproduce the experimental data well. Calculating the bound states from the K-matrix parameters obtained in that paper, would for some series, lead to states that had similar features as the experimental spectrum, but the principal quantum numbers of these models deviated significantly, see Fig. 4.4a and Fig. 4.6a. In the paper the

authors had also given a value for a χ^2_ν-test[1] of the fits. These values couldn't be reproduced either and lay much higher for some series. Exactly how theses deviations come about is not clear to us, as there is no documentation of the programmes used for fitting. However, we have checked these deviations with several people who have also observed them. To show some of these differences, we show our reproduction for the first three series, $^1S_0$, $^3S_1$ and $^1P_1$, of this paper. The first series does not show deviations, while the other two do.

[1] χ^2_ν is a statistical quantity, a fit can be considered to match the experimental data when $\chi^2_\nu \approx 1$ [16]. We will use it to conduct fits ourselves and give more detail in 5.1.

4.2 $^1S_0$ Series

We look at the Rydberg series consisting of the $5sns\,^1S_0$ states of strontium and two perturbing states. This series is particularly well suited for MQDT analysis because of the comparatively high quality of the spectroscopic data, with energy uncertainties as small as $0.001\,\mathrm{cm}^{-1}$[17]. This allows for a more precise fit.

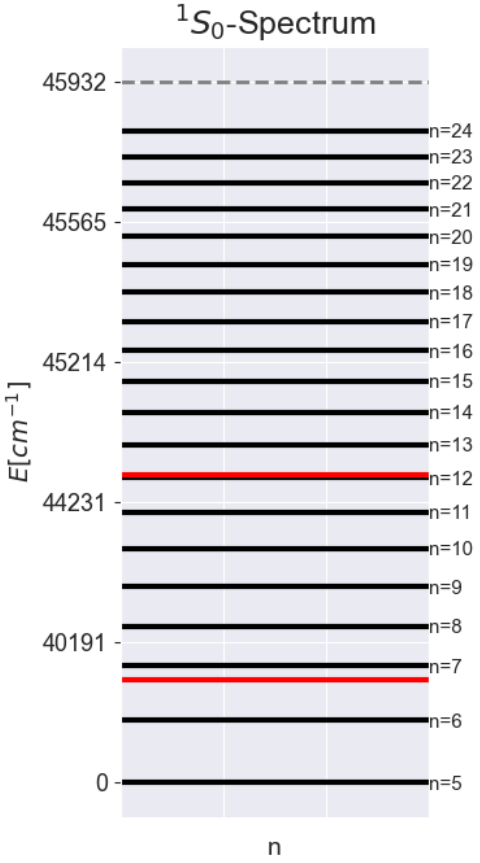

Figure 4.1: $5sns\,^1S_0$ spectrum with perturbers in red. The y-axis is scaled with n^{-3}.

Two perturbers due to doubly excited states are identifiable, one at $37\,160.234\,\mathrm{cm}^{-1}$ ($4d^2\ ^1S_0$) between the 5s6s and 5s7s states and a weak perturber at $44\,525.838\,\mathrm{cm}^{-1}$ ($4d^2\ ^3P_0$). They are depicted by red lines in Fig. 4.1. This series is best modelled with three channels $5s_{1/2}ns_{1/2}$, $4d_{3/2}nd_{3/2}$ and $4d_{5/2}nd_{5/2}$ which were labelled in jj coupling, with fine structure resolved ionisation limits. For a good fit, the low-lying states below n=7 were excluded, which is related to the fact that the approximations made in MQDT are only valid for certain distances from the atomic nucleus. Therefore only the $5sns\,^1S_0$ states with n between 7 and 30 taken from [17] and [18] , as well as the perturbing $4d^2\ ^3P_0$ state were used in the fit in the paper.

Fig. 4.2a shows our calculation of the bound state spectrum that ultimately results from the fitted K-matrix presented in [12], listed in Table 4.1. We

do get large deviations for the low lying state n=6 at $\nu_j \approx 1.92$ and the low lying perturber at $\nu_j \approx 2.17$, which were not included in the fit. On the other hand, the higher lying states including the perturber at $\nu_j \approx 2.62$ are well fitted. Using the K-matrix from the paper to calculate the spectrum, we observed $\chi^2_\nu = 0.39$, which indicates a good fit quality and is in agreement with the χ^2_ν value given in the paper.

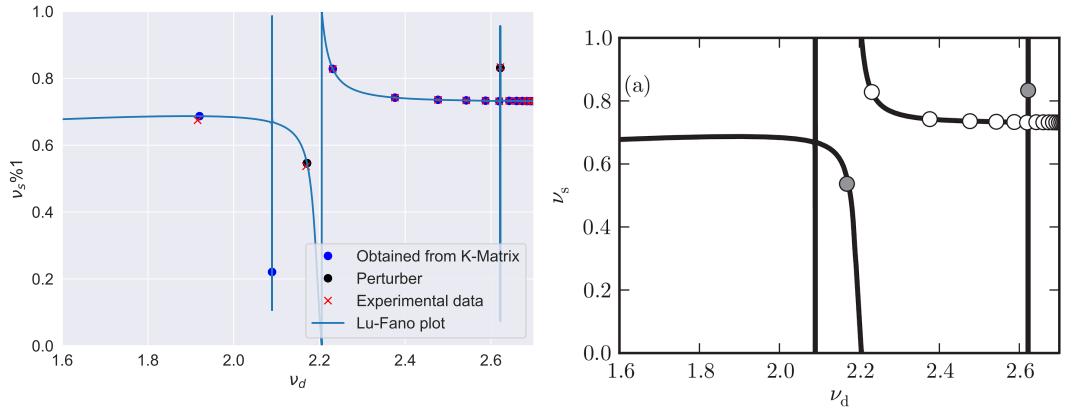

(a) Lu-Fano plot recreation. (b) Lu-Fano plot from [12].

Figure 4.2: $^1S_0$ Lu-Fano plot from [12] and our recreation.

Channel	1	2	3
Label	$5s_{1/2}ns_{1/2}$	$4d_{3/2}nd_{3/2}$	$4d_{5/2}nd_{5/2}$
Ionisation Limit	45 932.1982 cm^{-1}	60 488.09 cm^{-1}	60 768.48 cm^{-1}
K_{i1}	1.054	-0.023	0.370
K_{i2}	-0.023	2.9	0
K_{i3}	0.370	0	-0.66
$K_{ii}^{(1)}$	0.83	-13	0.51

Table 4.1: $^1S_0$ K-matrix fitting parameters from [12]. Coupling between perturbers was set to zero, $K_{23} = 0$.

This series represents a successful fit to the experimental data and the K-matrix was therefore successfully calculated. Next we look at two series from the same paper, where the K-matrix with our calculation did not reproduce the bound state spectrum well.

4.3 $^3S_1$ Series

This Rydberg series, consisting of the $5sns^3S_1$ states of strontium, displays no obvious resonance features. This is indicated by the fact that the bound states form a straight line in a Lu-Fano plot, see Fig. 4.4b. Older studies [19] also haven't found evidence that the series is perturbed. It may nonetheless be analysed using a two-channel model with channels labelled by $5sns^3S_1$ and $5pnp^3P_1$, since a $5p^{23}P_1$ state with an energy of $35\,400.105\,\mathrm{cm}^{-1}$ could perturb the series. The energy levels from n=7 to n=23 and no additional perturbers were included in the fit from the paper.

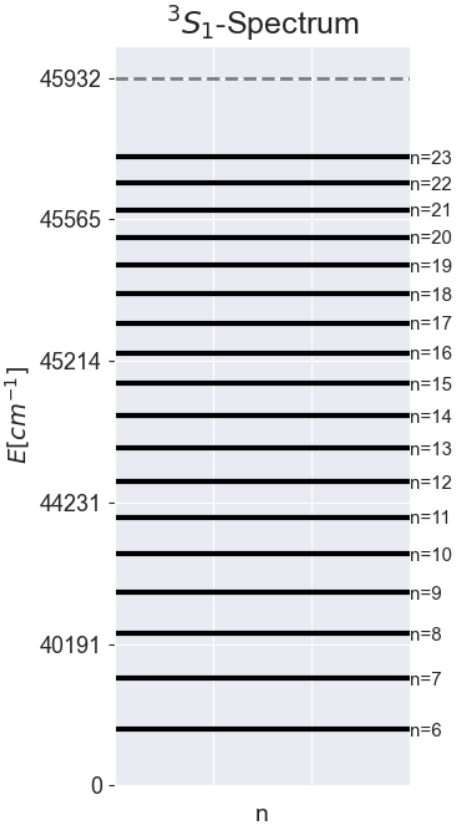

Figure 4.3: $5sns^3S_1$ spectrum with perturbers in red. The y-axis is scaled with n^{-3}.

However, when calculating the bound state spectrum from the K-matrix of the paper (Table 4.2), we observe strong deviations from the experimentally measured spectrum. In Fig. 4.4a the bound states lie noticeably below and to the left of the experimental data. Here the states that were obtained from the K-matrix seem to be off by upto 0.1 on the y-axis. Accordingly, $\chi^2_\nu \approx 2.9 \times 10^5$ even if the lowest two states at $37\,424.675\,\mathrm{cm}^{-1}$ and $40\,761.372\,\mathrm{cm}^{-1}$ are excluded. These large discrepancies occur despite the fact that this series has much larger error bars than previously in $^1S_0$, ranging from $0.01\,\mathrm{cm}^{-1}$ to $0.35\,\mathrm{cm}^{-1}$ [17]. The K-matrix is therefore not well fitted and does not reproduce the experimental data well.

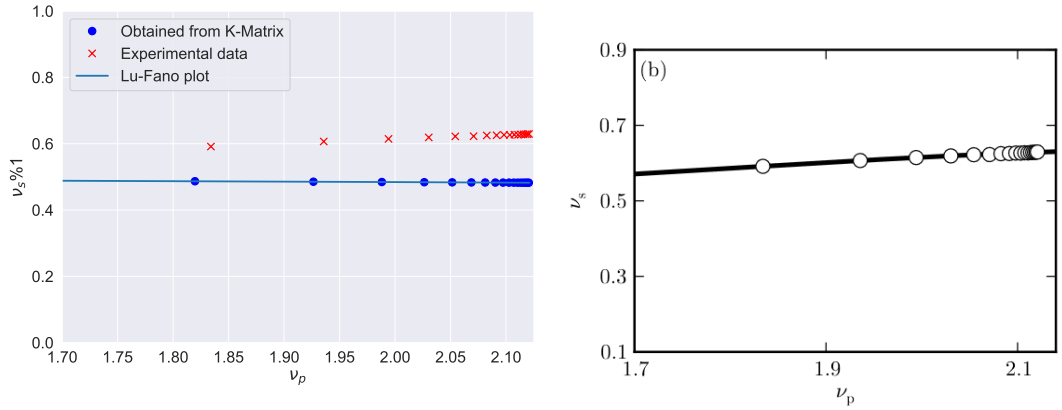

(a) Lu-Fano plot recreation.

(b) Lu-Fano plot from [12].

Figure 4.4: $^3S_1$ Lu-Fano plot from [12] and our recreation.

Channel	1	2
Label	$5sns^3S_1$	$5pnp^3P_1$
Ionisation Limit	$45\,932.1982\,\mathrm{cm}^{-1}$	$70\,048.11\,\mathrm{cm}^{-1}$
K_{i1}	-34.2	-155
K_{i2}	-155	-1470
$K_{ii}^{(1)}$	-19.14	-1408

Table 4.2: $^3S_1$ K-Matrix fitting parameters from [12]

4.4 $^1P_1$ Series

This Rydberg series, consisting of the $5snp^1P_1$ states of strontium, has a clearly visible perturbation, shown in Fig. 4.6b. This perturbation is due to a doubly excited perturber between the n=7 and n=8 states. The series is modelled with two channels in LS coupling, $5snp^1P_1$ and $4dnp^1P_1$, and a perturber labelled $4d5p^1P_1$ with an energy of $41\,172.054\,\mathrm{cm}^{-1}$. Spectroscopic data was taken from [17] with n = 6 to n = 29.

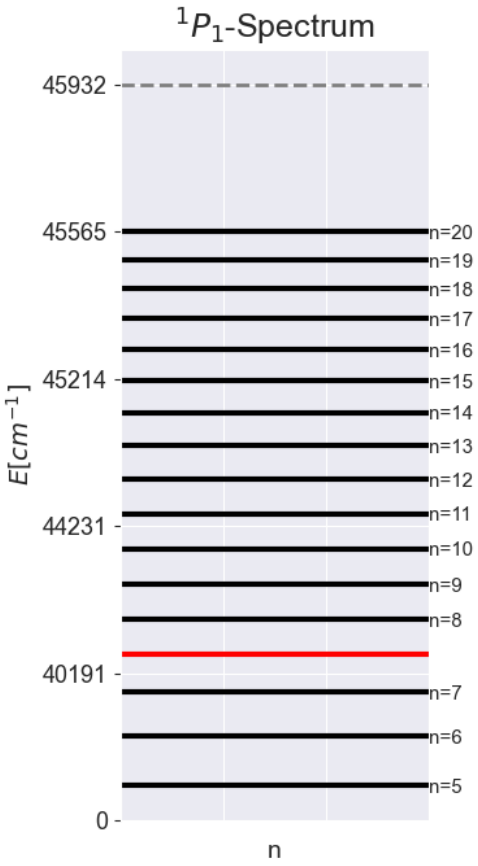

Figure 4.5: $5snp^1P_1$ spectrum with perturbers in red. The y-axis is scaled with n^{-3}.

Similarly to the $^3S_1$ series, when trying to reproduce the fit using the paper K-matrix (Table 4.3), we get a spectrum that is obviously not optimally fitted, and we again observe deviations between the experimental and the fitted spectrum. This is shown in Fig. 4.6a. The resulting χ^2_ν is as large as $\chi^2_\nu \approx 7.5 \times 10^7$ even if the low lying states at $21\,698.452\,\mathrm{cm}^{-1}$, $34\,098.404\,\mathrm{cm}^{-1}$ and $38\,906.858\,\mathrm{cm}^{-1}$ are excluded. Therefore, the $^1P_1$ Rydberg series is also not well fitted to experimental data.

Channel	1	2
Label	$5snp\,^1P_1$	$4dnp\,^1P_1$
Ionisation Limit	$45\,932.1982\,\mathrm{cm}^{-1}$	$60\,628.26\,\mathrm{cm}^{-1}$
K_{i1}	10.842	16.18
K_{i2}	16.18	22.56
$K_{ii}^{(1)}$	-0.39	1.68

Table 4.3: $^1P_1$ K-Matrix fitting parameters from [12].

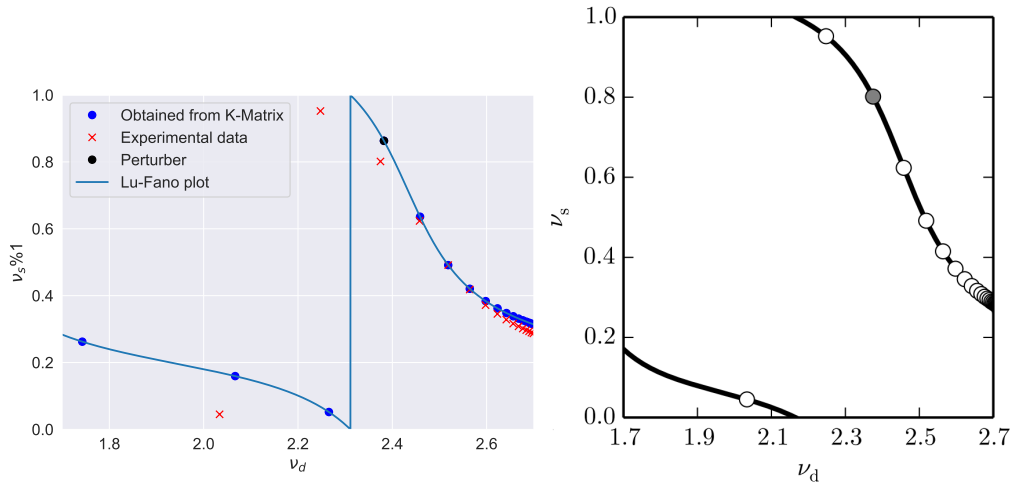

(a) Lu-Fano plot recreation.

(b) Lu-Fano plot from [12].

Figure 4.6: $^1P_1$ Lu-Fano plot from [12] and our recreation.

4.5 Summary

In this chapter we have looked at a 2014 MQDT analysis of strontium and reproduced the spectra using the K-matrix from the analysis. In total we have reproduced three series, by following the procedure explained in section 3.1.3. In two of them we observed a deviation of the spectrum from the experimental energies, indicated by the fact that $\chi^2_\nu \gg 1$, see Table 4.4:

Series	χ^2_ν	Properties
$^1P_1$	7.5×10^7	2 channels
$^3S_1$	2.9×10^5	2 channels
$^1S_0$	0.39	3 channels

Table 4.4: Summary of fitting results.

We know from various MQDT analyses that better fits are possible. In order to apply MQDT ourselves and gain an understanding of the fitting process, we will fit the K-matrices of these Rydberg series ourselves in the following chapter.

Chapter 5

Strontium K-Matrix Fit

The discrepancies we observed in the previous chapter between the spectra which were obtained via MQDT in [12] and their experimental values, made us attempt to fit the K-matrix ourselves. The quality of the resulting spectra can then serve as a benchmark for MQDT applied to strontium. We therefore chose the $^1P_1$, $^3S_1$ and $^1S_0$ series from the last chapter and aimed to obtain the respective K-matrices by fitting.

5.1 Fitting Procedure

To calculate the K-matrix of a Rydberg series, we fit the calculated spectrum belonging to the series to the experimentally measured spectrum. As introduced in section 3.2, we need to introduce a cost function, dependent on the K-matrix parameters, which measures how well the spectrum is approximated. This cost function is then minimised numerically by a minimisation algorithm.

Cost Function

We used the value χ^2_ν of the reduced chi-squared test as a cost function, which takes into account the calculated energies $E_i^{(calc)}$ and the measured

energies $E_i^{(exp)}$, as well as the uncertainties ΔE_i of the measured energies. It is evaluated by calculating the difference between the measured and the calculated energies, dividing by the uncertainties, and then squaring the value and adding them all up:

$$c_{cost}(K) = \chi^2 = \sum_{i=0}^{N} \left(\frac{E_i^{(calc)} - E_i^{(exp)}}{\Delta E_i} \right)^2 . \tag{5.1}$$

χ^2 is a statistical quantity that describes how well the calculated data fits the data observed in experiments. In general, a fit can be said to match the experimental data if $\chi^2_\nu \approx 1$ [16], where $\chi^2_\nu = \chi^2/\nu$ is the reduced chi-squared value, obtained by dividing χ^2 by the degrees of freedom ν of the model. ν is given by the number of experimentally observed data points, minus the number of fitting parameters.

A step in the fitting algorithm then looks as follows: In every fitting step we calculate the spectrum $\{E_i^{(calc)}\}$, which requires the principal quantum numbers $\{\nu_j\}$, since $E_i = I_i - \frac{\hat{R}}{\nu_i^2}$. The principal quantum numbers $\{\nu_j\}$ are obtained, as explained in section 3.1.3, by numerically calculating the zeros of the function $f(\nu_j) = \det\left(K_{i\alpha} + \delta_{i\alpha}\tan(\pi\nu_i(\nu_j))\right)$.

Next we calculate χ^2_ν, which is now possible since all $E_i^{(calc)}$, $E_i^{(exp)}$ and ΔE_i are known. This allows us to calculate the χ^2_ν for any K-matrix. The value of the cost function χ^2_ν depends only on the $\frac{N(N+1)}{2} + N$ entries of the K-matrix. We can therefore determine the K-matrix by minimising the cost function $c_{cost}(K)$ until $\chi^2_\nu \approx 1$, when the data is well fitted.

We wrote the fitting programme in Python 3 and implemented the procedure described in section 3.1.3 for finding bound states of a K-matrix. We implemented the cost function $c_{cost}(K)$ and used scipy.optimize for the actual minimisation, with the method set to use the Nelder-Mead algorithm for minimisation. A good choice of initial values was important to ensure convergence. Occasionally, we got cases where the amount of bound states did not match the number of experimental ones, making the calculation of

χ^2 impossible. In these cases we simply returned infinity as the value of c_{cost} to make these cases unfavourable in our minimisation.

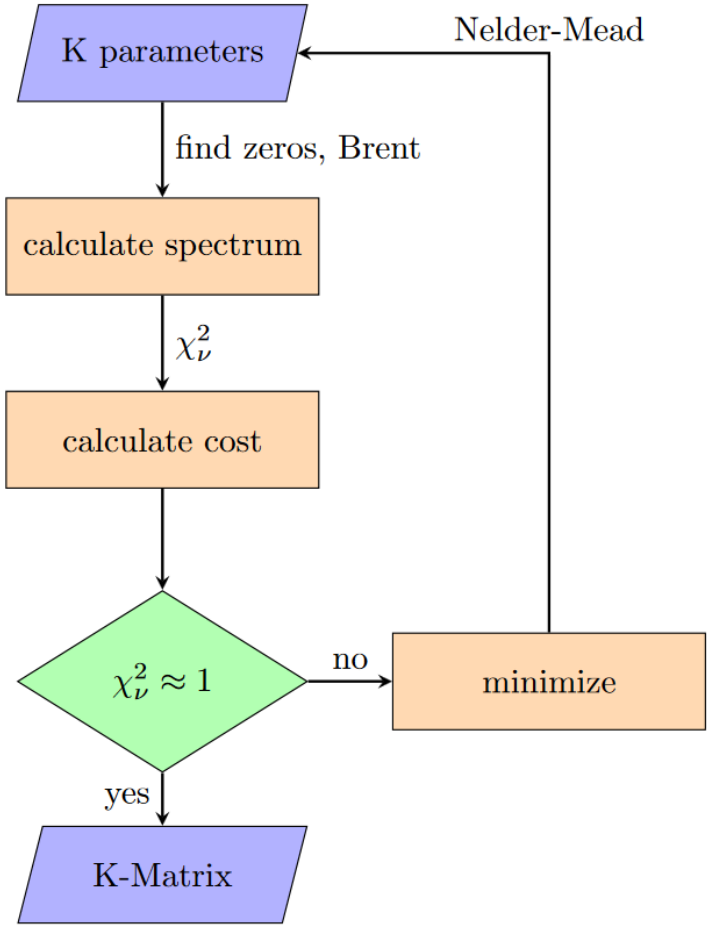

Figure 5.1: Flow chart of the empirical K-matrix fitting procedure.

Root finding

In order to find the roots of the function $f(\nu_j) = \det\left(K_{i\alpha} + \delta_{i\alpha}\tan(\pi\nu_i(\nu_j))\right)$, which is required in every fitting step, we looked at a region between the lowest and highest bound states of the fit. We divided it into small subintervals and looked for a root in each. This was done numerically, simply using the optimize.brentq algorithm, which is Scipy's implementation of Brent's

method for finding a zero of a function in an interval.

5.1.1 Spectroscopic Data

Experimental data for the Rydberg levels of strontium has been taken from [17] and [18] . Listing the energy levels and their respective experimental uncertainties relevant for our fit of the $^1P_1$, $^3S_1$ and $^1S_0$ series. We used ionisation limits from [12] and a Rydberg constant of $\hat{R} = \frac{\alpha^2 c m_e}{2h}\frac{M}{m_e+M} = 109\,736.627\,\mathrm{cm}^{-1}$.

5.2 $^1P_1$ Series

The structure of this two-channel series was discussed in the previous chapter, in Section 4.4. It has a perturber at $41\,172.054\,\mathrm{cm}^{-1}$ which leads to an avoided crossing in the region of $\nu_j \approx 2.2$, visible in the Lu-Fano plot, Fig. 5.2a. In the previous chapter we had observed deviations between the experimental spectrum and the spectrum calculated with the K-matrix published in [12].

For our own fit, we used the energies listed in Table B.1, from n=6 to n=20 around the avoided crossing. However, this resulted in large deviations between the fit and the experimental value for the n=10 bound state. Consequently, the n=10 level was excluded from the levels to which we fitted. As the result of this fit, we obtained the K-matrix for this Rydberg series, listed in Table 5.1. The fit converged to a value of $\chi^2_\nu = 1.60$ and an average deviation of the calculated states from the measured states of $\frac{\sum_i |E^i_{exp} - E^i_{theo}|}{N} = 0.03\,\mathrm{cm}^{-1}$. The individual levels obtained by our fit are listed in Table B.1. The spectrum is plotted in Fig. 5.2a and Fig. 5.2b.

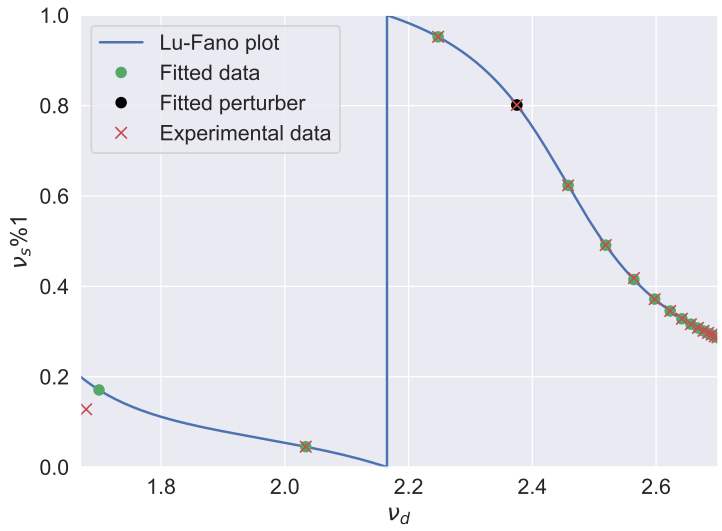

(a) $^1P_1$ fitting result over the whole fitted range

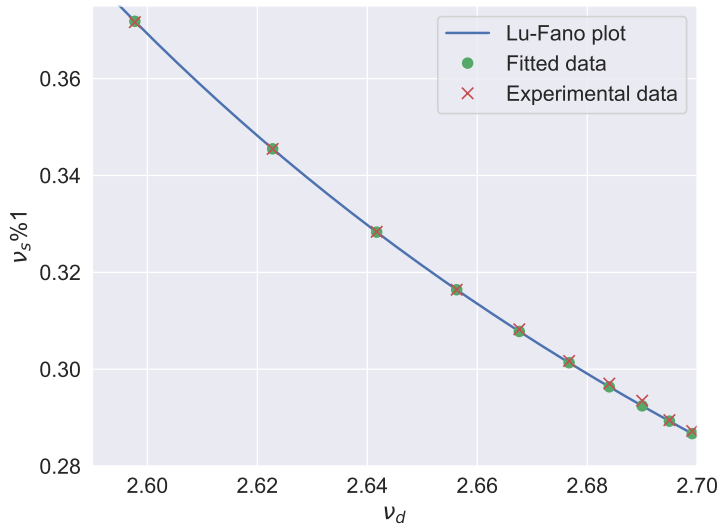

(b) $^1P_1$ fitting result plotted from ν_d =2.45 to ν_d =2.7

Figure 5.2

5.2.1 Channel Fractions

Using the K-matrix from our fit, we calculated the normalised channel fractions of the singlet P_1 series, proceeding as described in section 3.1.4. In Fig.

Channel i	1	2
Label	$5snp\,^1P_1$	$4dnp\,^1P_1$
Ionization Limit	$45\,932.1982\,\mathrm{cm}^{-1}$	$60\,628.26\,\mathrm{cm}^{-1}$
K_{i1}	11.08933826	-16.17747267
K_{i2}	-16.17747267	22.5548621
$K_{ii}^{(1)}$	0.38915608	1.67806199

Table 5.1: The $^1P_1$ K-matrix parameters as result of fit.

5.3 we plot the normalised channel fractions on the y-axis and the bound state energies on the x-axis. We can clearly see the influence of the $4d5p\,^1P_1$ perturber at $41\,172.054\,\mathrm{cm}^{-1}$ on the series, mixing into the wave function of the nearby bound states. However the $5snp\,^1P_1$ channel always makes the majority contribution to any given state.

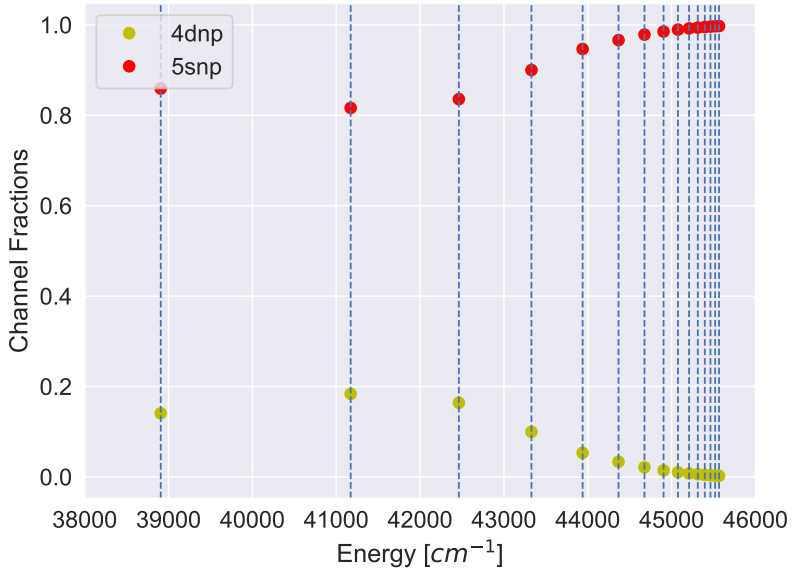

Figure 5.3: Channel fractions of the $^1P_1$ boundstates and perturbers.

5.3 $^3S_1$ Series

Next, we attempted to fit the triplet S Rydberg series, which is modelled by an unperturbed two-channel series, previously described in section 4.3. In the last chapter, we had observed large discrepancies between fitted and experimental energies with the K-matrix from [12]. The fitting procedure was similar to that of the $^1P_1$ case: We chose the states ranging from n=7 to n=23, listed in Table B.2 for the fit and, as this series is unperturbed, no perturbers had to be included.

Channel i	1	2
Label	$5sns^3S_1$	$5pnp^3P_1$
Ionisation Limit	$45\,932.1982\,\mathrm{cm}^{-1}$	$70\,048.11\,\mathrm{cm}^{-1}$
K_{i1}	-51.52265604	-193.05164398
K_{i2}	-193.05164398	-692.70163194
$K_{ii}^{(1)}$	30.08470079	-335.68290295

Table 5.2: The $^3S_1$ K-matrix parameters as result of fit.

The K-matrix entries obtained from this fit are listed in table 5.2. It converged to $\chi^2_\nu = 1.008$ and the calculated energies differ on average by $0.07\,\mathrm{cm}^{-1}$ from the experimental ones. The exact individual levels obtained by our fit are listed in Table B.2, and the resulting spectrum is plotted in Fig. 5.4a and Fig. 5.4b.

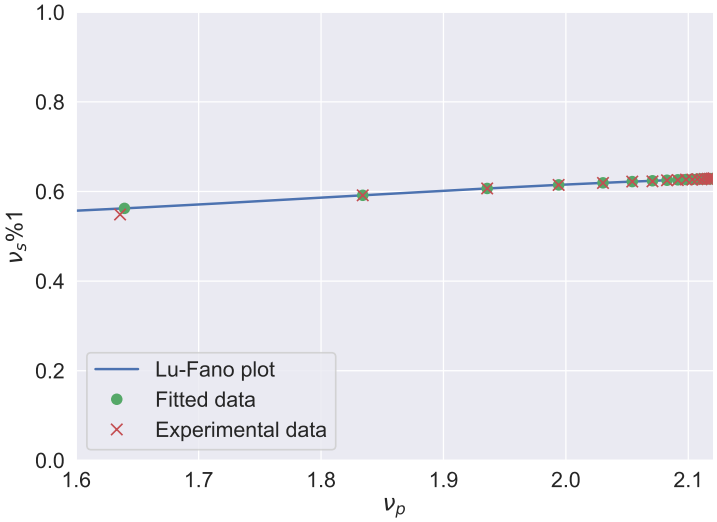

(a) $^3S_1$ fitting Result over the whole fitted range.

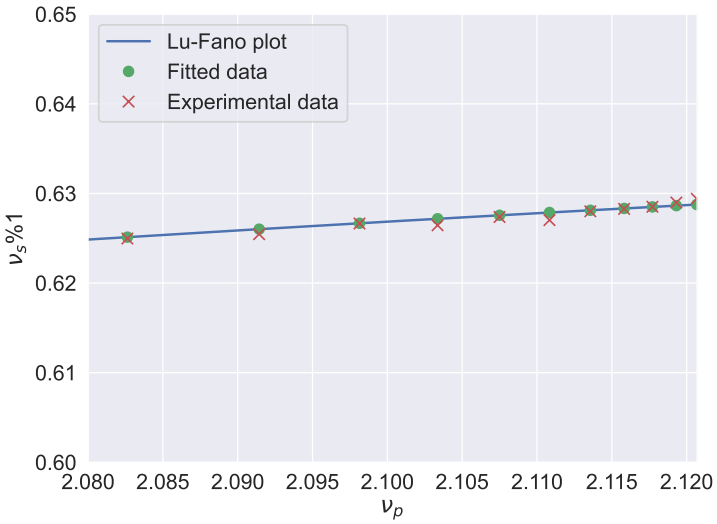

(b) $^3S_1$ fitting result from ν_p =2.080 to ν_p =2.120.

Figure 5.4

5.3.1 Channel Fractions

The channel fractions of this series are calculated for each of the bound states using the K-matrix obtained from fitting. They are plotted in Fig. 5.5. As

expected for this unperturbed series, we don't see any significant admixture of the second channel, as all states are almost completely pure, confirming the unperturbed nature of this series.

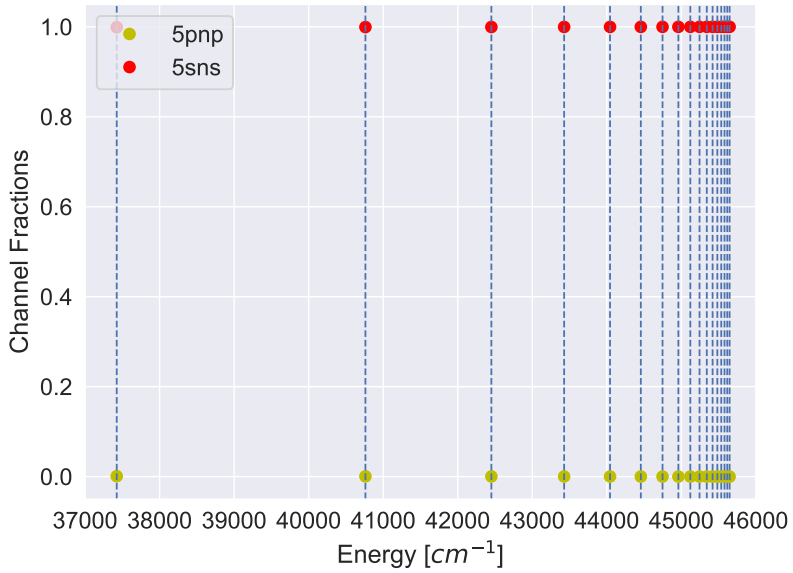

Figure 5.5: Channel fractions of the $^3S_1$ boundstates and perturbers.

5.4 $^1S_0$ Series

In the last chapter we observed good agreement between the theoretical K-matrix states of this series and the spectroscopic ones. However, we carried out our own fit to compare results. When we fitted this three-channel series, we included the levels from n=8 to n=30 listed in Table B.3 and the two perturbers at 37 160.234 cm^{-1} ($4d^2\ ^1S_0$) and at 44 525.838 cm^{-1} ($4d^2\ ^3P_0$).

The fit of this Rydberg series gave the K-matrix of Table 5.3, converging to $\chi^2_\nu = 0.48$. The average deviation of the calculated states from the measured states $\frac{\sum_i |E^i_{exp} - E^i_{theo}|}{N}$ is 0.0005 cm^{-1}. The individual levels obtained by our fit are listed in Table B.3 and the resulting spectrum is plotted in Fig. 5.6a and Fig. 5.6b.

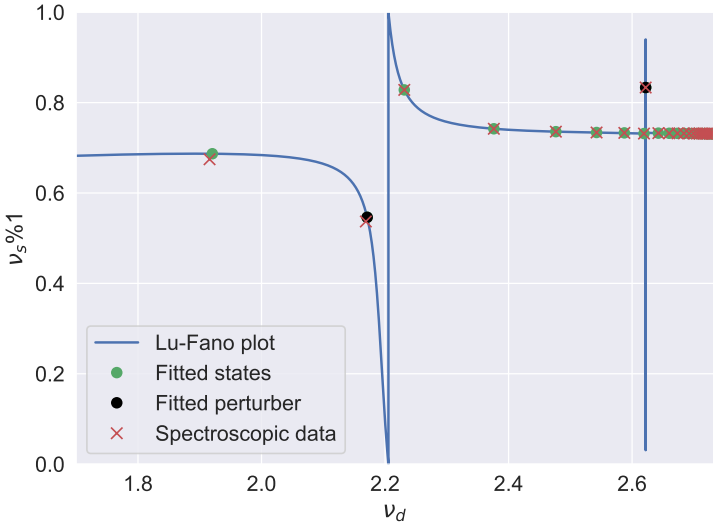

(a) $^1S_0$ fitting result over the whole fitted range.

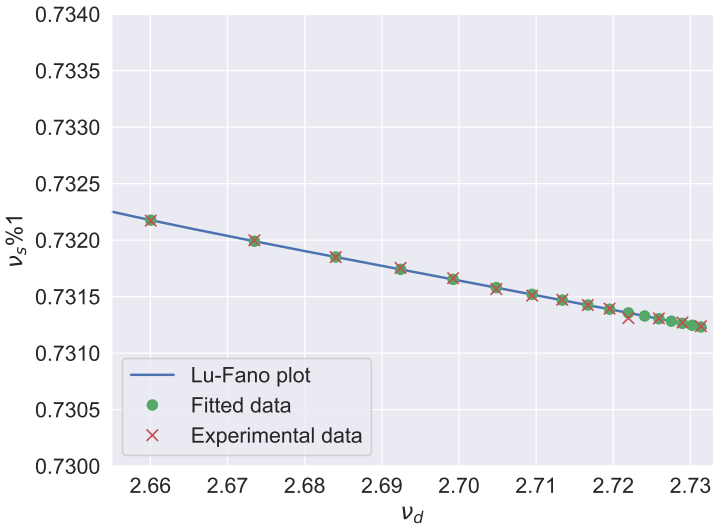

(b) $^1S_0$ fitting result from ν_d =2.65 to ν_d =2.735.

Figure 5.6

Channel i	1	2	3
Label	$5s_{1/2}ns_{1/2}$	$4d_{3/2}nd_{3/2}$	$4d_{5/2}nd_{5/2}$
Ionisation Limit	$45\,932.1982\,\mathrm{cm}^{-1}$	$60\,488.09\,\mathrm{cm}^{-1}$	$60\,768.43\,\mathrm{cm}^{-1}$
K_{i1}	1.05418009	-0.01958369	-0.37000828
K_{i2}	-0.01958369	2.02504807	0
K_{i3}	-0.37000828	0	-0.6619203
$K_{ii}^{(1)}$	0.82672574	14.90200058	0.50349886

Table 5.3: The $^1S_0$ K-matrix parameters as result of fit.

Our fitting result is comparable to the K-Matrix in [12], only the K_{22} entry differs by a value about of about 0.9, while all other entries are in agreement.

5.4.1 Channel Fractions

This series now has three channels as the basis for its channel fractions, which in jj coupling are labelled as $5s_{1/2}ns_{1/2}$, $4d_{3/2}nd_{3/2}$ and $4d_{5/2}nd_{5/2}$ with J=0. We can convert these channel fractions into LS-coupled channels, giving us $4dnd^3P_0$, $4dnd^1S_0$ and $5sns^1S_0$ for the quantum numbers of this series. To go from jj coupling to LS coupling, the transformation matrix is given by the standard Racah algebra of Equation 5.2 [12]:

$$\begin{aligned}\bar{A}_i^{(LS)} &= \sum_i \delta_{l_{1i'}l_{1i}}\delta_{l_{2i'}l_{2i}}\delta_{s_{1i'}s_{1i}}\delta_{s_{2i'}s_{2i}} \\ &\cdot \sqrt{(2j_{1i'}+1)\cdot(2j_{2i'}+1)\cdot(2L_i+1)\cdot(2S_i+1)} \\ &\cdot \begin{Bmatrix} l_{1i'} & s_{1i'} & j_{1i'} \\ l_{2i'} & s_{2i'} & j_{2i'} \\ L_i & S_i & J \end{Bmatrix} \cdot \bar{A}_{i'}^{(jj)}\,, \end{aligned} \tag{5.2}$$

which in this case can be expressed in a 3×3 transformation matrix:

$$\begin{bmatrix} 1 & 0 & 0 \\ 0 & \sqrt{\frac{3}{5}} & \sqrt{\frac{2}{5}} \\ 0 & -\sqrt{\frac{2}{5}} & \sqrt{\frac{3}{5}} \end{bmatrix} . \tag{5.3}$$

Using this matrix we can calculate the channel fractions in LS coupling, which are plotted in Fig. 5.7b. We see that the state mix due to the perturber at $37\,160.234\,\mathrm{cm}^{-1}$. The perturber at $44\,525.838\,\mathrm{cm}^{-1}$ has only has a small influence, mostly on the n=12 state.

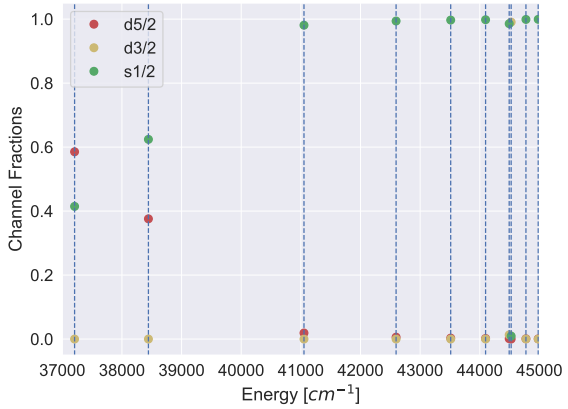

(a) Channel fractions $^1S_0$ in jj coupling.

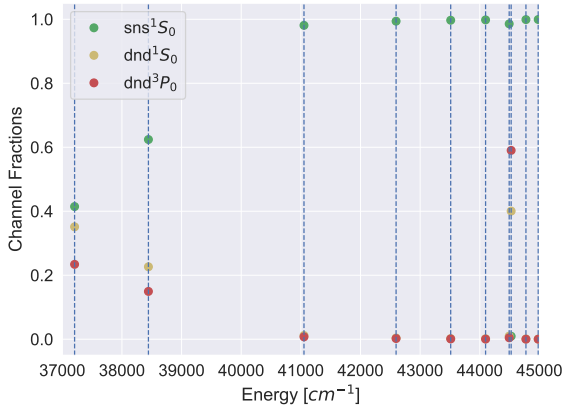

(b) Channel fractions $^1S_0$ in LS coupling.

Figure 5.7: Channel fractions in both coupling schemes.

5.5 Summary

In this chapter we have successfully applied MQDT to fit the K-matrix and channel fractions of the wave functions for three exemplary Rydberg series of strontium ($^1P_1$, $^3S_1$ and $^1S_0$). The resonance features of a given series are reproduced and the fits generally replicate their underlying data within their error bars (see: Table B.1, Table B.2 and Table B.3).

The channel fractions match our expectations about the composition of certain states and the admixture of perturbing levels. For example, showing that the $^3S_1$ is unperturbed.

Series	χ^2_ν	Properties
$^1P_1$	1.6	2 channels, n=10 excluded
$^3S_1$	1.0	2 channels, no perturber
$^1S_0$	0.48	3 channels, best spectroscopic data

Table 5.4: Summary of fitting results of the three Rydberg series.

However, there are limitations to MQDT: First is the fact, that the lower lying states cannot be reproduce and we often excluded one or two lower lying states of a series from a fit. The lowest state we included was in the $^1P_1$-Series, were we did include a state at $34\,098.404\,\mathrm{cm}^{-1}$, which in comparison to the other two series is a rather low lying state. This may explain why this series has the worst fit with $\chi^2_\nu \approx 1.6$. This discrepancy can be explained by the fact that the MQDT analysis relies on an approximation of the atomic potential as a Coulomb potential. This approximation is valid for electrons far from the atomic nucleus. Additionally, in the $^1P_1$ series we also had to exclude a state ($n = 10$) located at a higher energy of $43\,938.201\,\mathrm{cm}^{-1}$ from the fit.

A second important limitation of MQDT is its reliance on quality and quantity of available spectroscopic data, which limits the effectiveness of a χ^2_ν fit, as the fit will only be able to reproduce the spectroscopic data up to its respective uncertainties. However in order to identify weak perturbers, such

as $4d^2\,{}^3P_0$ in the ${}^1S_0$ series, good data is necessary. In general since MQDT is an empirical theory it can only be as good as its underlying data.

In the next chapter we will look at the MQDT studies that have been carried out on ytterbium.

Chapter 6

Ytterbium MQDT

Ytterbium

After conducting an MQDT fit for multiple strontium series, well will now turn out attention to ytterbium, another divalent atom which is widely used in many cold atom experiments [5], [20], [21]. It is an Alkaline-earth-like atom with atomic number 70 and isotopes ^{171}Yb (14.09%), ^{172}Yb (21.69%), ^{173}Yb (16.10%), ^{174}Yb (32.03%) and ^{176}Yb (13.00%) [22]. ^{171}Yb and ^{173}Yb have non-zero nuclear spins, however their effect are deemed small enough to not be considered.

6.1 Old MQDT Studies

There have been many works, featuring MQDT-Analysis of neutral ytterbium. These works feature many series with spectroscopic data of different quality. They are listed in Table 6.1.

Series	Source	Year
$6sns\,^1S_0$, $6snd\,^{1,3}D_2$	[23]	2018
$6sns\,^1S_0$, $6snd\,^{1,3}D_2$, $6snp\,^{1,3}P_1$	[24]	2015
$6snp\,^{1,3}P_1$, $6snp\,^3P_0$, $6snp\,^3P_2$, $6snf\,^{1,3}F_3$	[25]	1984
$6snp\,^3P_2$	[26]	1991

Table 6.1: MQDT studies of ytterbium series.

Notably, the triplet $6sns\,^3S_1$ series is missing and has yet to be analysed. Additionally, the older studies would benefit from newer and more precise spectroscopic measurements. This could be done in the lab this thesis was written in, the experiment is described in Appendix A.

6.2 MQDT Ytterbium

In terms of the theoretical description of Rydberg series of ytterbium, we can proceed as discussed in chapter 3. A series and its perturbers are described in terms of a K-matrix, obtained by fitting to the available spectroscopic data.

As a simple example, we can look at the fitted $6sns\,^1S_0$ series from [24]. This model for $6sns\,^1S_0$ Rydberg states features three channels with two perturbers. One perturber with an electron configuration of four unpaired electrons $4f^{13}5d6snp$ at $49\,897.32\,\mathrm{cm}^{-1}$ and one doubly excited perturber $6p^{21}S_0$ with an energy of $48\,344.38\,\mathrm{cm}^{-1}$. A fit with energy levels $10 \leq n \leq 65$ and no additional energy dependence ($\mu_1 = \mu_2 = \mu_3 = 0$) gave the K-matrix listed in Table 6.2. The resulting spectrum of this fit is shown in Fig. 6.1.

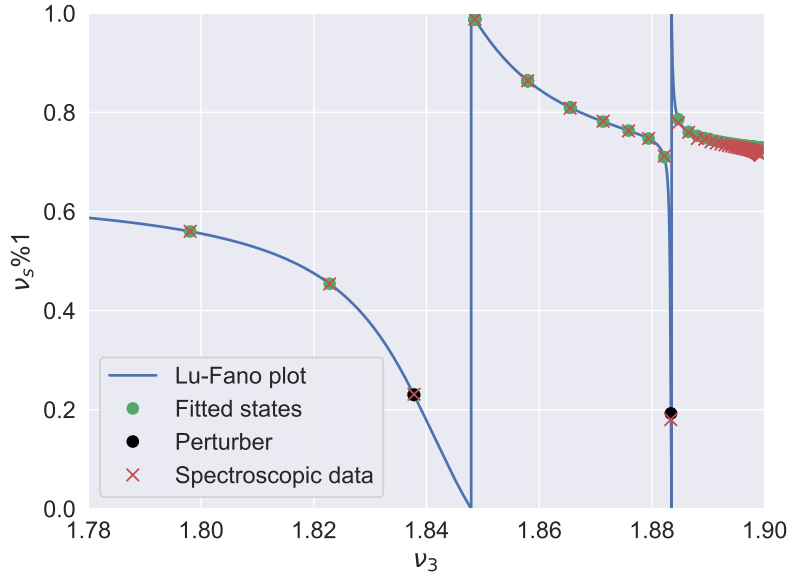

Figure 6.1: Lu Fano plot of 6sns$^1S_0$ with K-Matrix from [24].

Channel	1	2	3
Label	6sns$^1S_0$	$4f^{13}5d6snp$	$6p^{21}S_0$
Ionisation Limit	50 443.08 cm^{-1}	83 967.70 cm^{-1}	80 835.39 cm^{-1}
K_{i1}	2.06306	0.60349	-0.3390
K_{i2}	0.60349	1.09172	1.12e-8
K_{i3}	-0.3390	1.12e-8	0.38440

Table 6.2: $^1S_0$ fitting parameters from [24].

Chapter 7

Summary

In this thesis, we studied multichannel quantum defect theory. First we introduced the necessary theoretical background and showed that the K-matrix is the central quantity that encapsulates the complicated physics of the spectra of divalent atoms. We talked about how it can be fitted to spectroscopic data, following Fig. 5.1. Then we applied this fitting procedure to three strontium Rydberg series, successfully obtaining the K-matrix of each of the series, $^1P_1$, $^3S_1$ and $^1S_0$, listed in Tables 5.1, 5.2 and 5.3.

Series	χ^2_ν	Channels
$^1P_1$	1.6	2 channels
$^3S_1$	1.0	2 channels
$^1S_0$	0.48	3 channels

Table 7.1: Summary of fitting results.

We furthermore calculated the corresponding channel fractions 5.3, 5.5, 5.7b giving insight into the admixture of states that occurs in these divalent atoms. We also saw that as an empirical method MQDT is very much reliant on good spectroscopic data in order to reproduce a series with good precision and lower lying levels have to be excluded, due to the Coulomb approximation central to MQDT.

In ytterbium extensive MQDT studies have been conducted, however certain series are missing and in general the data is quite old and could be improved upon by newer measurements.

MQDT has many applications and has been applied to a hoist of physical problems, as well as a number of elements. It has been applied to cores with hyperfine splitting, Hydrogen molecules [27], low energy nuclear scattering and photofragmentation, molecular photoionization and photodissociation and low-energy collisions between an atom or molecule and an electron or another atom, to name a few [9].

However, there is no real unified approach and description of specifics, such as the used spectroscopic data, the concrete formulation of MQDT, or the fitting procedure are often lacking. It can also be difficult to get into MQDT for experimentalists, who would often benefit from MQDT calculations. To mitigate some of these things, we began to implement a Python library that in the future should allow for MQDT calculations. It was mostly design by Dr. Sebastian Weber and aims to implement MQDT for the divalent case discussed in this thesis, as well as for hyperfine split cores. It is designed in an open source fashion and will be hosted on Github. With the aim to catalogue spectroscopic data and K-matrix parameters, offering a Python library for performing MQDT fits.

Appendix A

Absorption Imaging

In addition to the work presented in the previous chapters of this thesis, an absorption imaging setup was built as part of this thesis. This imaging setup is part of an ultracold atom experiment, which among other things aims to realise the fast production of ultracold ytterbium atoms, utilizing a two-colour ytterbium MOT (magneto-optical trap) and to explore nonlinear quantum optics mediated by ytterbium Rydberg atoms.

The setup was built because absorption imaging allows to estimate values of atom number, atom density, temperature, shape and the position of the MOT-cloud and is therefore an important tool to evaluate the properties of the atoms trapped in the magneto-optical trap. We will now describe the construction of this imaging system and the underlying physical principles, starting with a basic description of important elements of the experiment.

The Ytterbium Experiment

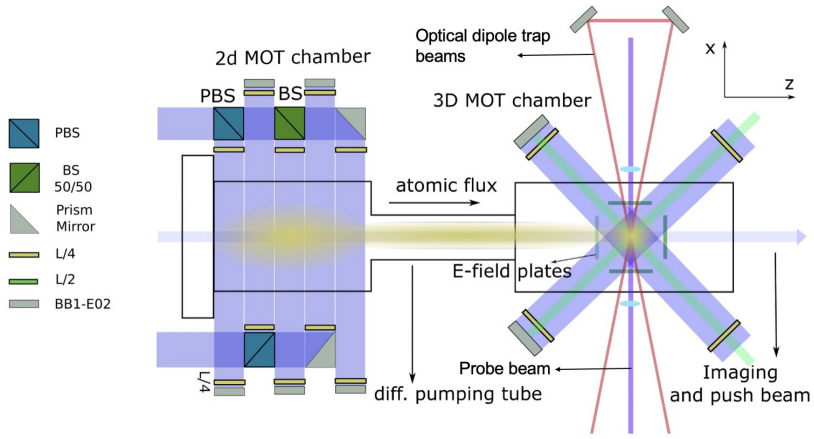

(a) Scheme of the experimental setup: The vertical imaging beam passes through the centre of the 3D MOT and out of the paper plane. The horizontal beam is the push beam.

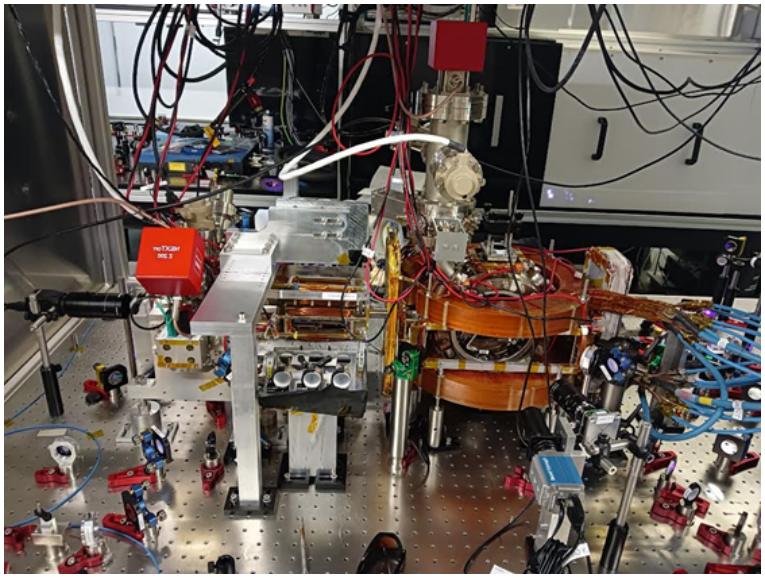

(b) Experimental setup: 2D MOT chamber on the left and 3D MOT chamber on the right, between the two magnetic MOT coils.

Figure A.1: Ytterbium MOT setup.

The experiment has two vacuum chambers, which are depicted in Fig. A.1a. One chamber contains a 2D MOT of ytterbium atoms and uses a push beam

to load the MOT of the second chamber. This second chamber features a two-colour 3D MOT where ytterbium atoms are trapped in three dimensions using two atomic transitions. One broad transition has a wavelength of 398.9 nm (blue) and a second narrow transition has a wavelength of 556 nm (green). This 3D MOT setup requires three green and three blue MOT beams, one for each spatial dimension. They are retroreflected and form the trap in the centre of the chamber.

Transition	Wavelength	Linewidth Γ	I_{sat}	T_{Doppler}
$6s^2\,{}^1S_0 \rightarrow 6s6p\,{}^1P_1$	398.9 nm	$2\pi \times 29.1$ MHz	$59.9\,\mathrm{mW/cm^2}$	$700\,\mu\mathrm{K}$
$6s^2\,{}^1S_0 \rightarrow 6s6p\,{}^3P_1$	555.8 nm	$2\pi \times 182$ kHz	$0.14\,\mathrm{mW/cm^2}$	$4.4\,\mu\mathrm{K}$

Table A.1: The two transitions used in the two-colour MOT [28].

After being trapped in the 3D MOT, the atoms can be transferred to a dipole trap for further probing and the preparation of Rydberg states.

In order to add a vertical imaging system to the setup, we had to consider that the vertical 3D MOT beams share a beam path with the laser beam that is used to image the cloud vertically. This can be seen in Fig. A.3a, where the vertical imaging beam is overlapped with a vertical green and a vertical blue MOT beam. All three beams pass through the centre of the MOT cloud along the y-axis of Fig. A.1a. However, the MOT beams need to be retroreflected, whereas the imaging beam needs to be transmitted to a camera. This can be implemented by using certain optical components, which will be described below.

Visible in Fig. A.1a, the setup features an additional horizontal imaging direction, simply using the push beam as an imaging beam. This beam is not overlapped with any other beams and it simply images the atoms onto a CCD camera, no separation optics are required. In the next section we describe the principles of the imaging technique we used, so called absorption imaging.

A.1 Absorption Imaging

To reliably quantify values of atom number, atom density, cloud shape and cloud position of the trapped atoms, we make use of absorption imaging. This involves measuring the intensity of a beam after it has passed through the atomic cloud at the wavelength of an atomic transition and allows one to make conclusions about the properties of the cloud mentioned above. We use the resonant transition from ${}^1S_0 \rightarrow {}^1P_1$ in ytterbium with a blue wavelength of 398.9 nm. This transition is used for imaging because it is identical to the MOT transition and we therefore have lasers at this wavelength readily available.

Physically, the technique of absorption imaging obeys the Lambert-Beer absorption law. It relates the optical density $OD(x, y)$ of an absorber in the imaging plane (in this case the atom cloud) to the intensity I of the imaging laser beam with initial intensity I_0:

$$I = I_0 e^{-OD(x,y)} = I_0 e^{-n(x,y)\sigma}, \tag{A.1}$$

with the on resonance cross section $\sigma = \frac{\hbar\omega\Gamma}{2I_{sat}}$ [29].

To measure the optical density, three camera images are taken during the experimental cycle: The first image is of the imaging beam without trapped atoms $I_{\text{full}}(x, y)$, the second is of the imaging beam being partially absorbed by the trapped atoms $I_{\text{cloud}}(x, y)$ and the third is a background image $I_{\text{back}}(x, y)$ without the imaging beam. This background image is subtracted from the other measurements so that the OD measurement is unaffected by background light. These three images are processed by a premade imaging software which automatically calculates the optical density in the camera plane and gives the total atom number of the trapped atoms by fitting Gaussians

along the x and y directions:

$$OD(x,y) = n(x,y)\sigma = \ln\left(\frac{I_{\text{full}} - I_{\text{back}}}{I_{\text{cloud}} - I_{\text{back}}}\right), \tag{A.2}$$

$$n_{atoms} = \frac{2\pi A_{\text{px,eff}}^2 \, OD_0 \sigma_x \sigma_y}{\sigma}, \tag{A.3}$$

σ_x and σ_y are the widths of the respective Gaussians and OD_0 the OD-peak. $A_{\text{px,eff}}^2$ is the effective pixel size of the camera, taking magnification into account.

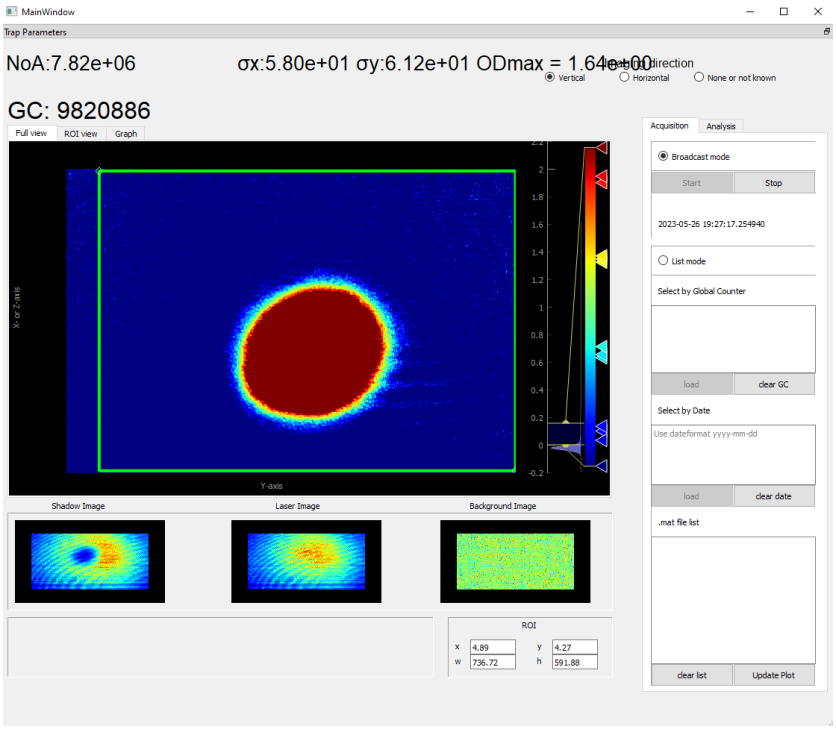

Figure A.2: Screenshot of the imaging software.

A.2 Imaging Setup

A.2.1 Beam Separation - Vertical Axis

As described above, the imaging beam on the vertical axis is overlapped with the green and blue MOT beams, which must be retroreflected to form

a MOT. To make imaging along this axis possible, we build a setup made up of the optics shown in Fig. A.3b. It consists of a quarter-wave plate (QWP), a dichroic mirror, a polarising beamsplitter, a mirror and a system of two lenses.

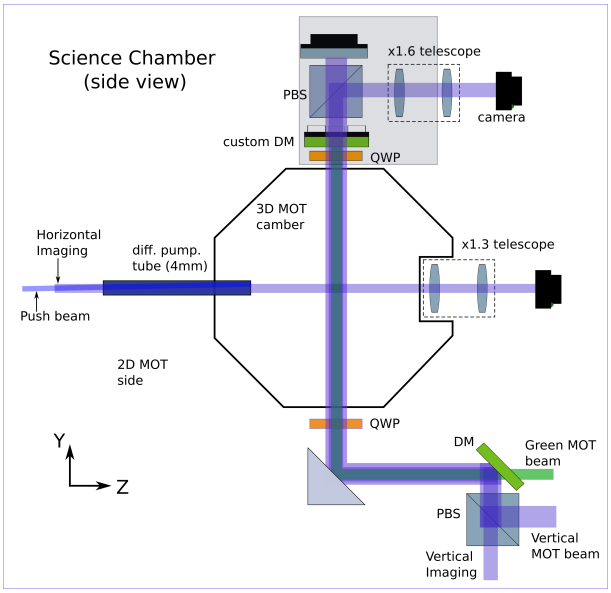

(a) Sketch shwoing the vertical and horizontal imaging setup.

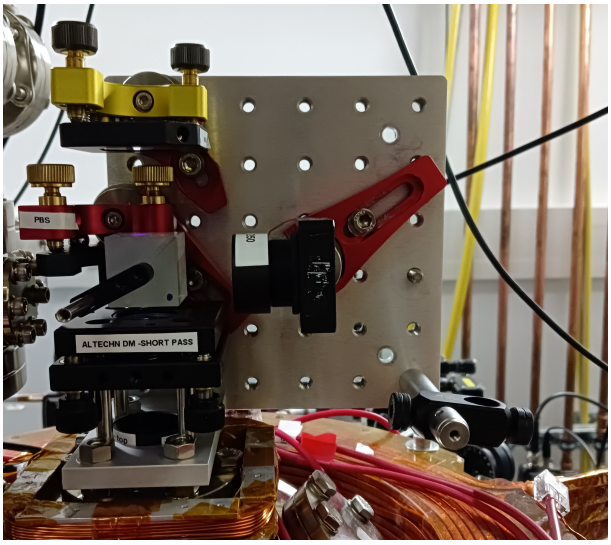

(b) Beam separation optics used in the experiment, before imaging onta a CCD

Figure A.3: Beam separation optics

Beam separation is now straightforward. As shown in Fig. A.3a, the three overlapped beams (green MOT, blue MOT and blue imaging) are sent vertically through the bottom viewport of the octagon and, after traversing the MOT cloud, enter the optics mounted atop the chamber. First, the green beam is reflected by a custom coded dichroic mirror, while the two blue beams are transmitted. Next, at a PBS both blue beams are now separated by their polarisation, as they have been made to have different linear polarisation after the QWP. The blue Mot beam enters the transmitting arm of the PBS and is reflected back into the chamber at a mirror. The imaging beam is reflected by the PBS and imaged onto a CCD camera. The QWP, through which the retroreflected beams pass twice, causes the circular polarisation of the MOT beams to flip from σ^+ to σ^-.

To mount the required optics, a breadboard on top of the science chamber, perpendicular to the experimental table, was chosen, as shown in Fig. A.3b. One could have chosen many methods for mounting these vertical optics, such as a cage system, but we ultimately used a simple breadboard. This allows great flexibility for possible future modifications, as most of the optical components can be mounted on a breadboard. Additionally, the optics are easy to place and the setup can be made compact. On the downside, the breadboard is quite heavy, however no significant vibrations have been noticed. The breadboard was mounted perpendicular to a base plate, into which the QWP is screwed. The base plate is depicted in Fig. A.4, it attaches to the chamber with four screws and was designed using Autodesk Inventor and manufactured in the Institute's workshop.

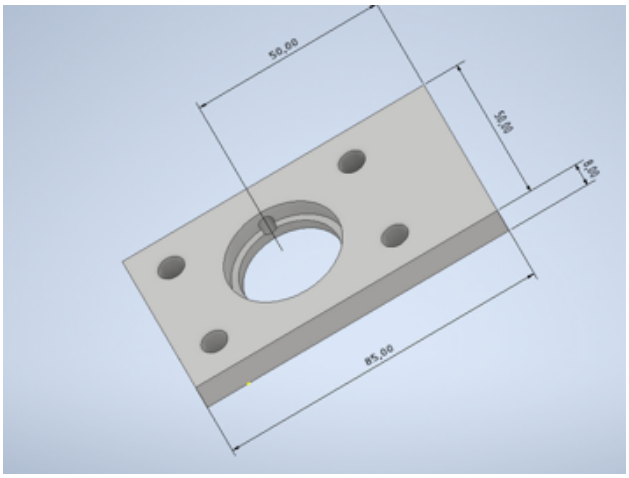

Figure A.4: Sketch of the base plate, designed in Autodesk Inventor. The large hole in the middle fits the QWP, the other four holes are used for mounting to the chamber.

A.2.2 Telescopes

Lastly, the beams on both axes, vertical and horizontal, had to be imaged onto a camera which was done using a simple Keplerian telescope, where they were also magnified to better match the size of the camera sensor.

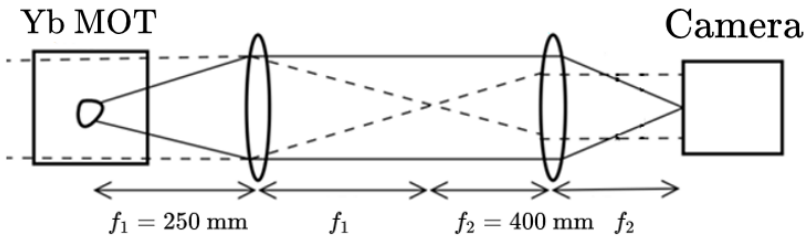

Figure A.5: Schematic of a Keplerian telescope., focal length of vertical axis.

However, when designing the system it is important to remember that the dimensions of the vacuum chamber impose a lower limit on the distance of the first lens from the MOT cloud, as the lens is placed outside the vacuum.

On the vertical axis, even with the relatively compact breadboard configu-

ration, the distance from the atom cloud to the first lens could not be made less than 250 mm. This results in a large distance between the objective and the eyepiece of the telescope, since in a telescope the distance between the two lenses is given by the sum of the focal lengths of the two lenses (f_1+f_2). Therefore we elected to chose a magnification of just $M = \frac{f_2}{f_1} = \frac{400\,\mathrm{mm}}{250\,\mathrm{mm}} = 1.6$ and get a rather long distance between the MOT cloud and the camera of $2f_1 + 2f_2 = 1300\,\mathrm{mm}$. The first lens, located on the breadboard, is chosen so that the cloud is in focus ($f = 250\,\mathrm{mm}$) and the second lens forms the eyepiece of the telescope($f = 400\,\mathrm{mm}$).

On the horizontal imaging axis, the structure of the chamber allows for a much shorter distance between the cloud and the objective lens. We built a second telescope and chose $f_1 = 150\,\mathrm{mm}$ and $f_2 = 200\,\mathrm{mm}$, leading to a magnification of $M = 1.3$.

Axis	$f_{\mathrm{objective}}$	f_{eyepiece}	Mag.	Res.	Eff. Pixelsize
Vertical	250 mm	400 mm	1.6	4.77 μm	4.03 μm
Horizontal	150 mm	200 mm	1.3	2.9 μm	4.85 μm

Table A.2: specifications of the telescopes on both axis, camera: pco.pixelfly usb.

All in all, this gives us the ability to perform reliable OD measurements of the two-colour ytterbium MOT and to produce biaxial absorption images, so that the MOT can be properly analysed and optimised in order to facilitate the optimal choice of experimental parameters. One such image from the experiment is depicted in Fig. A.6.

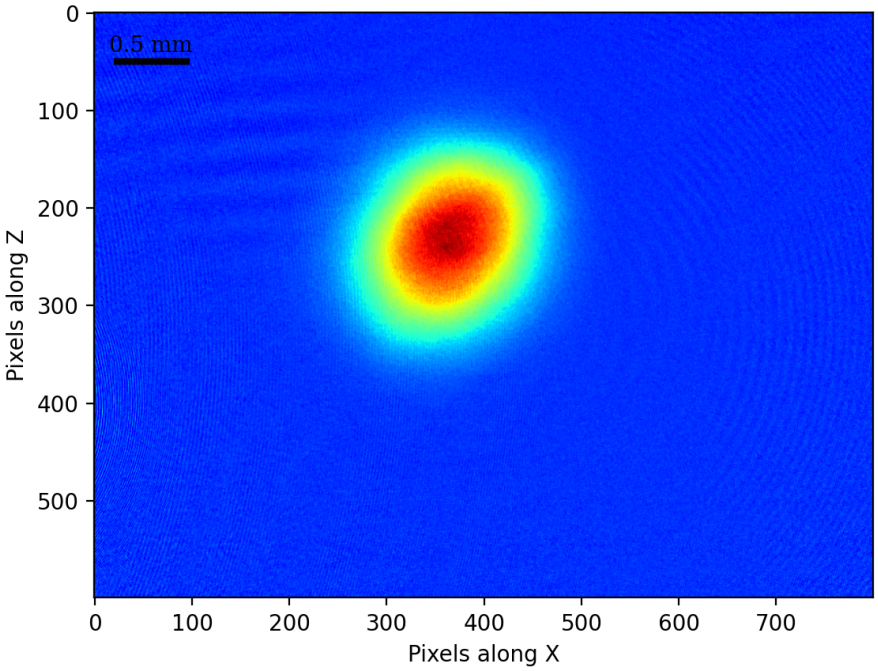

Figure A.6: Absorption image of a ytterbium MOT taken on the horizontal axis.

Appendix B

Fitting Data: $^1P_1$, $^3S_1$, $^1S_0$

n	E_{exp} [cm^{-1}]	Error [cm^{-1}]	E_{theo} [cm^{-1}]	Difference [cm^{-1}]	ν_d
5	21698.452	0.004	22645.359	9.5e+02	1.69973703
6	34098.404	0.006	34098.404	3.7e-06	2.03380053
7	38906.858	0.010	38906.858	2.3e-04	2.24766651
4d5p	41172.054	0.014	41172.055	8.9e-04	2.3749077
8	42462.136	0.014	42462.137	6.6e-04	2.45778944
9	43328.04	0.07	43327.90	1.4e-01	2.51853635
10	43938.201	0.025	43936.394	1.8e+00	2.5640315
11	44366.42	0.03	44366.49	6.8e-02	2.59771723
12	44675.737	0.029	44675.744	7.3e-03	2.62277607
13	44903.50	0.03	44903.49	1.4e-02	2.64170065
14	45075.29	0.03	45075.29	9.3e-04	2.65625108
15	45207.83	0.04	45207.78	5.3e-02	2.66763749
16	45311.99	0.04	45311.96	3.3e-02	2.6766946
17	45395.34	0.04	45395.29	5.1e-02	2.68400612
18	45463.02	0.05	45462.95	6.5e-02	2.68998728
19	45518.64	0.03	45518.63	1.1e-02	2.69493864
20	45565.00	0.03	45564.98	2.2e-02	2.69908147

Table B.1: Comparison of experimental and calculated energies for $^1P_1$.

n	E_{exp} [cm^{-1}]	Error [cm^{-1}]	E_{theo} [cm^{-1}]	Difference [cm^{-1}]	ν_p
6	29038.773	0.004	29218.019	1.8e+02	1.63940264
7	37424.675	0.005	37424.675	2.0e-05	1.83404911
8	40761.372	0.020	40761.370	1.7e-03	1.93570998
9	42451.16	0.35	42451.32	1.6e-01	1.99409821
10	43427.44	0.19	43427.66	2.2e-01	2.03033691
11	44043.35	0.20	44043.31	3.6e-02	2.05423004
12	44456.25	0.21	44456.68	4.3e-01	2.0707539
13	44747.65	0.15	44747.69	3.8e-02	2.08262904
14	44960.22	0.15	44960.32	1.0e-01	2.0914362
15	45120.41	0.15	45120.41	3.7e-03	2.09814129
16	45243.88	0.15	45243.96	7.9e-02	2.10336005
17	45341.28	0.15	45341.30	1.7e-02	2.10749928
18	45419.29	0.15	45419.35	5.9e-02	2.11083616
19	45482.89	0.01	45482.90	6.6e-03	2.11356463
20	45535.32	0.01	45535.32	2.5e-03	2.11582358
21	45579.08	0.01	45579.08	7.6e-04	2.11771455
22	45615.99	0.01	45615.98	1.2e-02	2.1193131
23	45647.40	0.01	45647.38	1.9e-02	2.12067641

Table B.2: Comparison of experimental and calculated energies for $^3S_1$.

n	E_{exp} [cm^{-1}]	Error [cm^{-1}]	E_{theo} [cm^{-1}]	Difference [cm^{-1}]	$\nu_{d3/2}$
6	30591.825	0.016	30731.736	1.4e+02	1.92037455
$5p^2$	37160.234	0.005	37206.193	4.6e+01	2.17103398
7	38444.013	0.007	38444.013	6.0e-06	2.23115552
8	41052.324	0.019	41052.324	4.4e-04	2.3761561
9	42596.572	0.022	42596.574	1.9e-03	2.47657926
10	43512.1658	0.0010	43512.1659	1.1e-04	2.54248905
11	44097.1224	0.0010	44097.1219	4.8e-04	2.58745915
12	44492.8348	0.0010	44492.8349	1.2e-04	2.6192697
$4d^2$	44525.838	0.010	44525.838	1.4e-04	2.62197605
13	44773.6707	0.0010	44773.6715	7.7e-04	2.64257088
14	44979.4540	0.0010	44979.4548	7.9e-04	2.66004518
15	45134.9242	0.0010	45134.9231	1.1e-03	2.67347925
16	45255.2295	0.0010	45255.2296	7.7e-05	2.68401583
17	45350.2296	0.0010	45350.2285	1.1e-03	2.69242453
18	45426.5505	0.0010	45426.5498	7.3e-04	2.69923757
19	45488.7860	0.0010	45488.7867	7.5e-04	2.70483178
20	45540.2024	0.0010	45540.2029	5.4e-04	2.70947969
21	45583.1688	0.0010	45583.1687	1.3e-04	2.71338212
22	45619.4391	0.0010	45619.4391	1.4e-05	2.71668961
23	45650.3365	0.0010	45650.3363	1.5e-04	2.71951667
24	45676.8704	0.0010	45676.8715	1.1e-03	2.72195167
25	-	-	45699.8287	-	2.72406362
26	45719.8235	0.0010	45719.8234	6.2e-05	2.72590705
27	-	-	45737.3442	-	2.72752547
28	45752.7832	0.0010	45752.7831	1.03e-04	2.72895397
29	-	-	45766.4572	-	2.73022106
30	45778.6257	0.0010	45778.6256	8.1e-05	2.73135012

Table B.3: Comparison of experimental and calculated energies for $^1S_0$.

Bibliography

[1] T. F. Gallagher, *Rydberg Atoms*. Cambridge Monographs on Atomic, Molecular and Chemical Physics, Cambridge University Press, 1994.

[2] J. Lim, H.-g. Lee, and J. Ahn, "Review of cold rydberg atoms and their applications," *Journal of Korean Physical Society*, vol. 63, pp. 867–876, 08 2013.

[3] N. Šibalić and C. S. Adams, *Rydberg Physics*. 2399-2891, IOP Publishing, 2018.

[4] H. Levine, A. Keesling, G. Semeghini, A. Omran, T. T. Wang, S. Ebadi, H. Bernien, M. Greiner, V. Vuletić, H. Pichler, and M. D. Lukin, "Parallel implementation of high-fidelity multiqubit gates with neutral atoms," *Phys. Rev. Lett.*, vol. 123, p. 170503, Oct 2019.

[5] S. Saskin, J. T. Wilson, B. Grinkemeyer, and J. D. Thompson, "Narrow-line cooling and imaging of ytterbium atoms in an optical tweezer array," *Phys. Rev. Lett.*, vol. 122, p. 143002, Apr 2019.

[6] D. J. Griffiths and D. F. Schroeter, *Introduction to Quantum Mechanics*. Cambridge University Press, 3 ed., 2018.

[7] M. Marinescu, H. R. Sadeghpour, and A. Dalgarno, "Dispersion coefficients for alkali-metal dimers," *Phys. Rev. A*, vol. 49, pp. 982–988, Feb 1994.

[8] A. Sanayei, N. Schopohl, J. Grimmel, M. Mack, F. Karlewski, and J. Fortágh, "Quasiclassical quantum defect theory and the spectrum of highly excited rubidium atoms," *Phys. Rev. A*, vol. 91, p. 032509, Mar 2015.

[9] M. Aymar, C. H. Greene, and E. Luc-Koenig, "Multichannel rydberg spectroscopy of complex atoms," *Rev. Mod. Phys.*, vol. 68, pp. 1015–1123, Oct 1996.

[10] G. Drake, *Springer Handbook of Atomic, Molecular, and Optical Physics*. Springer Handbook of Atomic, Molecular, and Optical Physics, Springer New York, 2005.

[11] F. Richtmyer and E. Kennard, *Introduction to Modern Physics, by F.K. Richtmyer and E.H. Kennard*. International series in physics, McGraw-Hill, 1947.

[12] C. L. Vaillant, M. P. A. Jones, and R. M. Potvliege, "Multichannel quantum defect theory of strontium bound rydberg states," *Journal of Physics B: Atomic, Molecular and Optical Physics*, vol. 47, p. 155001, jul 2014.

[13] M. J. Seaton, "Quantum defect theory i. general formulation," *Proceedings of the Physical Society*, vol. 88, p. 801, aug 1966.

[14] W. E. Cooke and C. L. Cromer, "Multichannel quantum-defect theory and an equivalent n-level system," *Phys. Rev. A*, vol. 32, pp. 2725–2738, Nov 1985.

[15] M. S. Child, *MQDT normalization*, p. 273–277. Cambridge Molecular Science, Cambridge University Press, 2011.

[16] I. Hughes and T. Hase, *Measurements and Their Uncertainties: A Practical Guide to Modern Error Analysis*. OUP Oxford, 2010.

[17] J. E. Sansonetti and G. Nave, "Wavelengths, Transition Probabilities, and Energy Levels for the Spectrum of Neutral Strontium (SrI)," *Journal of Physical and Chemical Reference Data*, vol. 39, 08 2010. 033103.

[18] R. Beigang, K. Lücke, A. Timmermann, P. West, and D. Frölich, "Determination of absolute level energies of 5sns1s0 and 5snd1d2 rydberg series of sr," *Optics Communications*, vol. 42, no. 1, pp. 19–24, 1982.

[19] R. Beigang, K. Lücke, D. Schmidt, A. Timmermann, and P. J. West, "One-photon laser spectroscopy of rydberg series from metastable levels in calcium and strontium," *Physica Scripta*, vol. 26, p. 183, sep 1982.

[20] A. Jenkins, J. W. Lis, A. Senoo, W. F. McGrew, and A. M. Kaufman, "Ytterbium nuclear-spin qubits in an optical tweezer array," *Phys. Rev. X*, vol. 12, p. 021027, May 2022.

[21] C. W. Hoyt, Z. W. Barber, C. W. Oates, T. M. Fortier, S. A. Diddams, and L. Hollberg, "Observation and absolute frequency measurements of the $^1s_0{-}^3p_0$ optical clock transition in neutral ytterbium," *Phys. Rev. Lett.*, vol. 95, p. 083003, Aug 2005.

[22] M. Berglund and M. E. Wieser, "Isotopic compositions of the elements 2009 (iupac technical report)," *Pure and Applied Chemistry*, vol. 83, no. 2, pp. 397–410, 2011.

[23] H. Lehec, A. Zuliani, W. Maineult, E. Luc-Koenig, P. Pillet, P. Cheinet, F. Niyaz, and T. F. Gallagher, "Laser and microwave spectroscopy of even-parity rydberg states of neutral ytterbium and multichannel-quantum-defect-theory analysis," *Phys. Rev. A*, vol. 98, p. 062506, Dec 2018.

[24] A. Zuliani, *Vers la manipulation optique d'atomes ultra-froids d'ytterbium excités dans des états de Rydberg.* Theses, Université Paris Saclay (COmUE), Nov. 2015.

[25] M. Aymar, R. J. Champeau, C. Delsart, and O. Robaux, "Three-step laser spectroscopy and multichannel quantum defect analysis of odd-parity rydberg states of neutral ytterbium," *Journal of Physics B: Atomic and Molecular Physics*, vol. 17, p. 3645, sep 1984.

[26] W. Bi-ru, Z. You-feng, X. Yun-fei, P. Li-gang, L. Ji, and Z. Jian-wei, "The 6snp 3p0.2 rydberg series of neutral ytterbium," *Journal of Physics B: Atomic, Molecular and Optical Physics*, vol. 24, p. 49, jan 1991.

[27] S. Ross and C. Jungen, "Quantum-defect theory of double-minimum states in h_2," *Phys. Rev. Lett.*, vol. 59, pp. 1297–1300, Sep 1987.

[28] J. Lee, J. H. Lee, J. Noh, and J. Mun, "Core-shell magneto-optical trap for alkaline-earth-metal-like atoms," *Phys. Rev. A*, vol. 91, p. 053405, May 2015.

[29] T. Pyragius, "Developing and building an absorption imaging system for ultracold atoms," 2012.

Declaration of Originality

I confirm that the submitted thesis is original work and was written by me without further assistance. Appropriate credit has been given where reference has been made to the work of others. The thesis was not examined before, nor has it been published. The submitted electronic version of the thesis matches the printed version.

Eidesstattliche Erklärung

Hiermit versichere ich an Eides statt, dass ich die vorliegende Arbeit selbstständig und ohne die Benutzung anderer als der angegebenen Hilfsmittel angefertigt habe. Alle Stellen, die wörtlich oder sinngemäß aus veröffentlichten und nicht veröffentlichten Schriften entnommen wurden, sind als solche kenntlich gemacht. Die Arbeit ist in gleicher oder ähnlicher Form oder auszugsweise im Rahmen einer anderen Prüfung noch nicht vorgelegt worden. Ich versichere, dass die eingereichte elektronische Fassung der eingereichten Druckfassung vollständig entspricht.

Köln, den 05. Juni 2023

Jonas Cieslik